

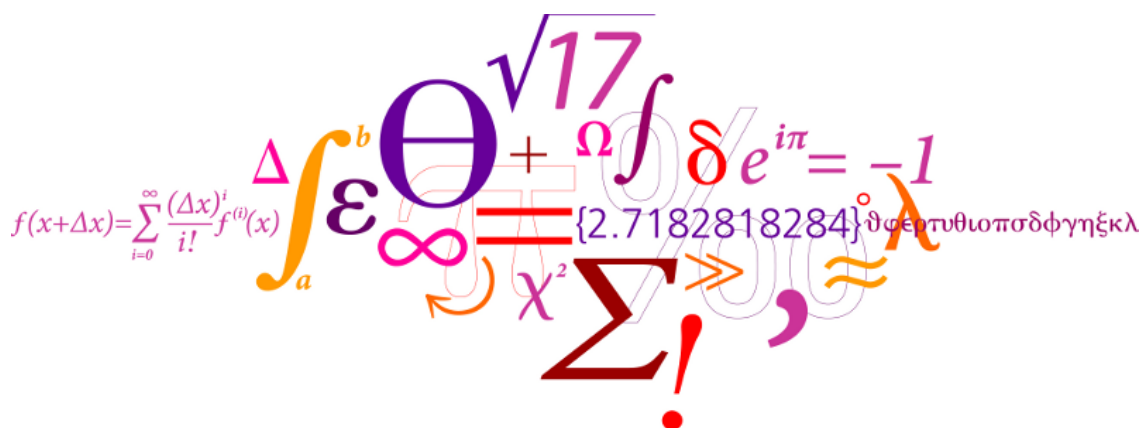
MICROCOMPUTER

PROJECT REPORT

by

KATLEEN BLANCHET s150798

TITOUAN BOULMIER s150810



December 11, 2015



Technical University of Denmark
Department of Electrical Engineering

Contents

Introduction	1
Context	1
Problem formulation	2
Problem delimitation	3
1 Theory Section	5
1.1 Mars Features	5
1.1.1 Atmosphere of Mars	5
1.1.2 Climate of Mars	7
1.1.3 Albedo	7
1.2 State of Art of the Depth Mapping	7
1.2.1 Principal Techniques Based on Image Analysis	8
1.2.2 M-array Pattern Projection Method [9]	10
1.2.2.1 Pattern Disorders	10
1.2.2.2 Correction of Pattern Disorders	10
1.2.3 Grid Indexing	13
1.2.3.1 Mini-patterns Used as Code Words	13
1.2.3.2 2D Array of Color-coded Dots	13
1.3 Image processing	15
1.3.1 HSV Color System	15
1.3.2 Morphological Operations [3]	15
1.3.2.1 Erosion	16
1.3.2.2 Dilation	16
1.3.2.3 Opening	17
2 Development	18
2.1 Scene Analysis	18
2.1.1 Camera	18
2.1.1.1 CCD	18
2.1.1.2 Field of View	19
2.1.1.3 Focal Length	19

2.1.1.4	Aperture	20
2.1.2	Artificial Light Source	21
2.1.2.1	Design of the Light Source	22
2.1.2.2	Validation of the Light Source	23
2.1.3	Signal Noise Ratio	24
2.1.3.1	Irradiance	24
2.1.3.2	Target's Radiance	25
2.1.3.3	Target's Irradiance	25
2.1.3.4	Light Source Irradiance	26
2.1.3.5	Signal/Noise Ratio	27
2.1.4	Summary and Comparison with MER Cameras	31
2.2	Distance Camera-Target of One Point	31
2.3	Image Processing	34
2.3.1	Color Detection	35
2.3.2	Beams Distinction	37
2.3.3	Centroiding	39
3	Experimental Results	43
3.1	Distances with Several Points	43
3.1.1	Choices of Implementation	43
3.1.2	Progress of the Experiment	44
3.1.3	Results	46
3.1.4	Interpretations	48
3.1.5	Limits of the Experiment	49
A	LED Properties	50
B	CCD Properties	51

Introduction

Context

The research of habitable planet is one of the major concerns of human beings. Indeed, this discovery, in addition to giving hope of locating another species, would bring solutions to overpopulation. According to scientists, the main criterion for life is water. Since the properties of celestial bodies are disparate, a habitable zone has been defined, considering that water can only exist at a specific range of temperature. If the temperature of the planet is too low, the water will freeze and conversely, it will evaporate if the temperature is too warm. The habitable zone is not fixed; it moves with the evolution of the sun. Mars is thought to have belonged to the zone once, due to its most hospitable climate after Earth. For a matter of fact, NASA's Mars Reconnaissance Orbiter has recently provided a strong evidence of water currently flowing on the Red Planet. It may then be possible to live on Mars and that is the aim of Mars one project: send a colony over there. The terraforming, which would change characteristics of Mars to make it suitable for humans, is also worth considering before colonization. In order to do so, scientists need to learn more about the features of the planet. Orbiters and rovers are already scanning mars surface and soil. Nevertheless, they lack the depth information, only equipped of Two Dimensional (2D) cameras. Their three dimensional (3D) scans have permitted to acquire it and to print a Martian meteorite on Earth in 2014. This information is useful for a better understanding of the rocks properties but that is not enough. Some missing data have delayed the 3D print. It could be interesting to provide to scientists a real time 3D map of a selected rock. It would be easier to study stones but the map could also help the robot to stabilize. With wind and an uneven ground, the rover is liable to move. The pattern recognition of a rock would be more robust by adding a 3D map. Samples could be collected being sure that the robot has taken the right piece.

Furthermore, the 3D map could have several other applications. The features of the Martian soil acquired by the orbiting satellites are not exhaustive and lack of accuracy. Thus, applied to the area in front of the robot, the 3D map could detect new obstacles and update in real time the available map to distinguish modifications of the ground. It could also permit spacecrafts to determine a flat area to land in real time by analyzing the surface of the planet from space and during the descent. Moreover, the 3D map can be applied in completely different fields. Indeed, this technique can be found, for example, in video games with environment recordings for real time augmented reality gaming, in medicine with skin surface or skin roughness measurement, in cosmetic with wrinkle measurement

and also in industry with 3D-automated optical inspection, volume measurement or classification of grinding materials and tools.

However, the 3D mapping is not very common and is still improving. In this context, designing a system capable of carrying out a 3D map of a Martian rock would be profitable for future research. This is the purpose of this project, undertaken during the Image Analysis with Microcomputer course, under the supervision of Alessandro Massaro. Combining image and scene analysis, programming and robotics seems relevant for learning to work as an engineer.

This report is intended to our fellow students. The first part will bring additional knowledge required to understand the next developments. The design of the system is described in the next section, followed by its verification. To end, future work is addressed.

Problem formulation



Figure 1: Curiosity Rover with an embedded camera on a arm [10]

In this report, we assume that we would like to send a rover on Mars, capable of communicating with Earth. Self-powered by solar panels, it will land at latitude 50° where it could get enough sunlight to recharge its lithium batteries. It is provided with an arm whose hand is replaced with a camera (see figure 1). The latter will be used by scientists to observe relevant rocks to study. In order to accomplish this mission, once a stone is designed, the camera must be able to keep it in focus, despite the wind, the movement of the robot or any other perturbation. This implies a real time image analysis to be able to rectify the position of the camera. As a robust method is needed to maintain the stone in front of the arm, the identification of patterns should be completed by carrying out a 3D map of

the surface. A luminous source should then be added to the rover to be projected on the surface containing the rock and detected by the camera.

This luminous source must be powerful enough to outshine the sunlight during the day, notwithstanding that the energy needed to make it work has to be negligible compared to the amount provided to the rover. Moreover, the characteristics of the camera need to be perfectly adapted to Mars, as once the rover has landed on the red planet, it would be impossible to adjust it.

Will it be feasible to design such an embedded system, composed of a camera, a luminous source and algorithms, capable of keeping a rock in focus thanks to a 3D map, for an application on Mars soil?

Problem delimitation

First of all, we assume that the rover is already in front of the rock, that is to say, we do not take into account the path to go close to the target with the different potential obstacles that may be present on the way. Then, in order to design the rover's camera which will be used to study rocks and to implement a robust algorithm to carry out a 3D map of the rock's surface, different characteristics of Mars and of the target need to be specified. However, as all of them cannot be taken into account, some simplifications and choices will be assumed.

Mars delimitation

Plenty of missions on Mars have been realized and a great deal of data has already been gathered. Nevertheless, even if some of them will be used to design our system, others will be simplified or even ignored. The first simplification concerns the atmosphere of Mars. Indeed, even if its composition is now well known, it will be assumed that the dirt on the surface of Mars plus the different layers of the atmosphere absorb, or scatter, 10% of the solar energy. Moreover, the influence on the image acquisition that the dirt between the target and the camera could have will not be taken into account. The second reduction covers the temperature. Indeed, even if it can reach -143°C during winter, 27°C during summer and have around 60°C variations between daytime and nighttime[12], we will assume that the CCD sensor works well all the time.

Target delimitation

Regarding the target, that is to say the part of the rock being studied, it is supposed to :

- be vertical;

- not exceed 2*2 meters
- have an area between 0.1 and 1 square meters;
- have a relief less than meters.

Camera delimitation

Then, regarding the camera which is designed during this study, it is presumed to :

- be between one and two meters far from the target;
- be right in front of the target, that is to say that the angle between the normal of the target's surface and the focal axis of the camera is 0° ;
- be able to capture the image of a target of 2 meters height maximum.

The different characteristics of target and the camera are represented figure 2

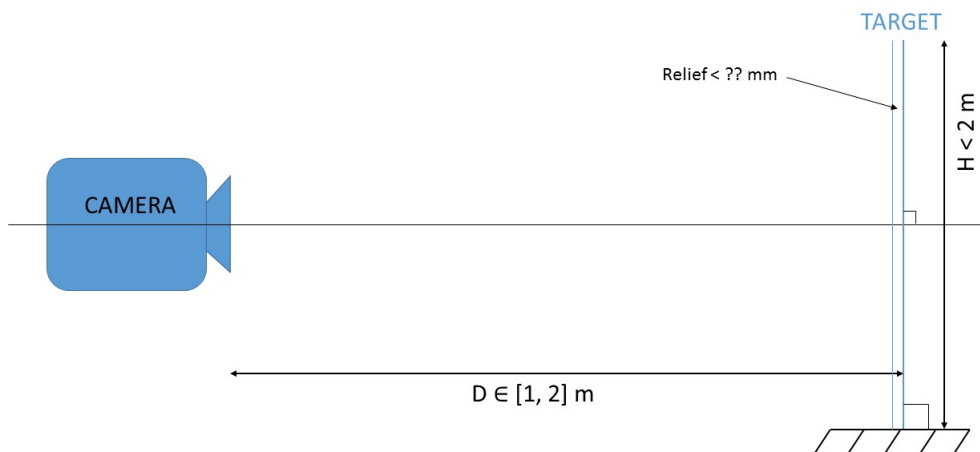


Figure 2: Schema of the scene

Finally, the last assumption is that the wave length taken into account is from 400 to 800 nm . Indeed, the first reason is that the CCD sensor chosen (see part 2.1.1.1) works with this range of wave length. Moreover, this range corresponds almost to the visible spectrum (380 - 750 nm), with which the 3D algorithm works, and as Mars has a reddish color and a lot of infrared, the spectrum is expanded to 800 nm .

Part 1

Theory Section

1.1 Mars Features

Mars, the fourth planet from the Sun (1.3814 to 1.6660 AU) is the second smallest planet of the the Solar System (its radius is 3389.5 km). Known as the “Red Planet” because of the amount of iron oxide on its surface, it has an orbital period of 668.6 sols (Mars’ solar day), that is to say 687 days, with an average day length of 24h37m.

1.1.1 Atmosphere of Mars

Because of its thin atmosphere, Mars has surface features which present analogies with both Moon, through the impact craters, and Earth, with volcanoes, deserts, polar ice caps. It is mainly composed of carbon dioxide CO_2 (96,0 % \pm 0,7 %), argon Ar (1,93 % \pm 0,01 %) and oxygen O_2 (0,145 % \pm 0,009 %). As the gravity of Mars is low, the height of the atmosphere is 11 km, more than one and a half times higher than the Earth’s one (7 km). Moreover, due to this low gravity, the wind can disrupt a rover easier than on Earth and a large amount of suspended dust is perpetually present at the surface.

Regarding the dust, of which the particles have a mean diameter of $1,5\mu\text{m}$, is continually injected into the atmosphere by wind or dust devils (a 12 km high one can be seen in Figure 1.1). Such eddies are far from anecdotal because they bring dust to significant volumes of the atmosphere. Even if the amount of dust is never very massive, it can be lifted by winds slower than 2 m/s and maintained indefinitely by wind of only $0,8\text{ m/s}$.

Moreover, regarding the wind on Mars, in low altitudes, the Hadley circulation¹ dominates and is almost the same process which, on Earth, generate the Trade winds. In high altitudes, a battery of areas of high and low pressure,

¹movement on a planetary level of the layers of gases surrounding the planet



Figure 1.1: Dust Devil. Mars Reconnaissance Orbiter, made by HiRISE on Feb. 16, 2012 [2]

named baroclinic pressure waves², dominates the weather. The Mars wind lift a large amount of dust and can even trigger huge dust storms which can affect the whole atmosphere (see Figure 1.2). Cyclonic storms can also appear on Mars. Indeed, cyclones similar to the ones of Earth tend to create during summer in the northern hemisphere but only in high latitudes.



Figure 1.2: Two views of Mars with spatial telescope Hubble before and after the big dust storm in 2001 [1]

²In meteorology a baroclinic atmosphere is one for which the density depends on both the temperature and the pressure

1.1.2 Climate of Mars

Because of its distance to the Sun bigger than the one of Earth, Mars receives less solar energy 2.1.3.1. Additionally, as its atmosphere is thinner, there is only a negligible greenhouse effect, and hence the average temperature is around -63°C on the surface of Mars with wide variations between daylight and night.

Then, the obliquity of Mars is close to the one of Earth (respectively $25,19^{\circ}$ and $23,44^{\circ}$) but the eccentricity of Mars is bigger (0,09332 against 0,01671 for Earth) which means that, if Mars has similar seasons to Earth, they have different intensity and duration during the martian year. Thus, the northern hemisphere has seasons less pronounced than the southern hemisphere because its aphelion is at the end of spring and its perihelion at the end of autumn. Thus, there are short and soft winters and long and fresh summers in the northern hemisphere. On the opposite, the southern hemisphere has very pronounced seasons with long and cold winters and short and warmer summers than in the northern hemisphere. That is why there are higher temperature differences in the south.

1.1.3 Albedo

Mars surface is covered by sand and volcanic rocks. The first purpose of this project is to allow scientists to examine these rocks through the camera. To achieve it, it is needed to know their characteristics, especially their albedo. As a reminder, the albedo is the fraction of incident light which is reflected from a surface. We can assume that the power reflection of Martian rocks is the same than on Earth. Then, to cover a wide range of rocks, the albedos of a black and of a white stone would be considered. Charcoal, as a dark rock, is a powerful absorber of the sun radiation, with an albedo around 0.05. On the contrary, chalks are poor absorbers and their albedo reach 0.45 according to [7]. In the following parts of the report, it will be taken for granted that Martian rocks have an albedo between 5 and 45%.

1.2 State of Art of the Depth Mapping

Traditional cameras only take 2D pictures, with horizontal and vertical information. To reproduce the human vision useful in various applications such as the stabilisation of a Martian rover harm in front of a rock to be analysed, it is often needed to add the depth data to get 3D coordinates of each pixel of the images. The depth mapping, also called 3D surface measurement or 3D imaging techniques etc, is carried out by two non-contact major methods as specified by [11]: “projecting (in the active form) or acquiring (in the passive form) electromagnetic energy onto/from an object followed by recording the transmitted or reflected energy”. They can be divided into two categories, the non-optical and optical sensing. The first one generally uses acoustic and electromagnetic sensors to determine the distance from the system to the object, by assessing the duration of a round trip of a pulse. In the latter the light permits to get the depth. We will focus on this last technique as it will be more convenient to achieve it on Mars. Active optical sensing uses an additional light source where as passive optical sensing works only with the irradiance reaching the scene and the radiance of the object.

1.2.1 Principal Techniques Based on Image Analysis

We will address only methods using image analysis as this is the purpose of the course.

Stereo vision and Photogrammetry systems are passive. The principle of the first is based on the utilisation of two or more cameras to record the scene. The reconstruction of the 3D is carried out by solving a correspondance problem with the identification of patterns in two or several images. The photogrammetry method calculates the depth by taking pictures from different points of view of a scene, through a camera preliminary calibrated. Both techniques demand a high computing power. Thus they are dismissed since the Rover cannot provide too much power to the embedded processor.

In active optical sensing, laser triangulators and structured light can be distinguished. They share the same approach: a beam or a pattern is projected through a laser source towards the object and its position on the image acquired by the camera is measured. Then, the distance from the camera to the object (the depth) is found by applying a triangulation technique. The difference between the two methods is that it is needed to scan the whole object for the laser triangulators one. Indeed, only a beam or a laser strip reaches it. The experiment has to be repeated several times to have an exhaustive 3D map. Regarding the structured light approach, unique patterns are projected simultaneously which allows to obtain the depth data at once if the object is small but in any case, it reduces a lot

the number of acquisitions compared to the laser triangulators. According to [4], the patterns can be in 3D but they are rare. 2D patterns are the most common and easier to implement. Depending on the scene motion, the structured light method can be classified into multi-shot and single-shot. If the scene is moving, the acquisition time must be short and thus, one picture should be enough to get the desired information. On the other hand, if no constraint is given, several pictures can be taken and a pattern adapted to sequential can be selected. In our case, the scene does not move but the robot arm needs to be stabilised and could move. That is why only single-shot structured light will be considered.

In the future part of the report, the implementation and experiments will be performed through laser triangulators techniques. They are easier to set up but will only give us a partial depth map. To obtain a complete 3D map in a single shot, structured light should then be applied to the martian rock. A method that could be carried out then is described below.

1.2.2 M-array Pattern Projection Method [9]

The binary M-array pattern projection method consists in projecting dark and light dots. The color of each dot represents a 0 (dark) or 1 (light) of the M-array pattern. The spatial coordinates of each dot matched with a projected one of the pattern can be determined by triangulation. However, pattern disorders occur often in the observed pattern and some dots cannot be matched. One of the asset of this method is the detection and correction of pattern disorders.

1.2.2.1 Pattern Disorders

According to [9], there are three different types of pattern disorder.

- Deficiency of dots. If there are several objects in the scene, an object may obstruct the pattern. On the Figure 1.3, the first, second and third dots are not visible by the camera.
- Displacement due to Difference in Depth : in comparison to the initial pattern projected, the dots may shift because of the depth of each object. On the Figure 1.3, the dots 4 to 6 on the object 2 have shifted to the left compared with the dots of object 1.
- Permutation of dots : if an object is in front of another, the order of dots may change. On the Figure 1.3, the dot 3 has changed of order and is the fourth one from the point of view of the camera.

1.2.2.2 Correction of Pattern Disorders

There are four steps in the matching of the observed dots with those of the pattern and the correction of the pattern disorders.

Temporary Array

The image recorded is analyzed line per line of dots and a 2-D array which contains the numbers of the observed dots is created. The array can be computed by these steps :

- Creation of the array (all the elements are set to zero).
- Scan of the image to detect dots. Each time a dot is found, its value and position (center) are saved into 1-D arrays VALUE, X and Y.
- The position of the dots are quantized using X and Y so that adjoining dots have consecutive quantized coordinates.

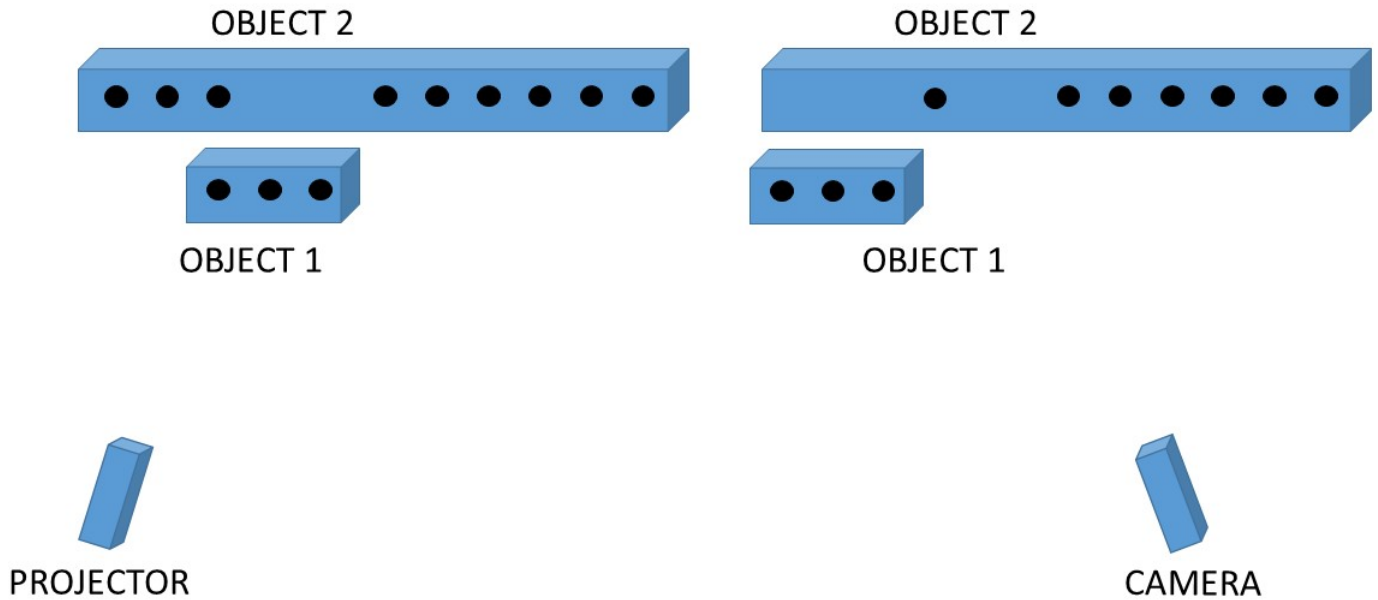


Figure 1.3: Pattern Disorders

- Insertion of the number of each dot into the array (the location into the array corresponds to the quantized coordinates).

This temporary array (T-array) may have some vacant places due to disorder pattern.

Grow

Each element of the T-array gets an index (column number of the M-array). To do so, a window is defined and applied to the T-array and the M-array where the elements into the window of each array have the same value. The element into the window of the T-array can be indexed using the M-array and the two windows moved simultaneously by one column or row. This is repeated until a difference between the two windows is detected. New windows are then initialized elsewhere. The grow terminates when no window can be initialized to an area of the T-array where there is no index yet.

Correction of Pattern Disorders

The detection step is carried out during the growing and is explained below using an example. We use a 3×4 window.

- step 1 : the region growing starts at $(0',0')$ and $(0,0)$ on the T-array and M-array (see Figure 1.4 a).
- step 2 : the window slides to the right until a difference between the two arrays is detected (see Figure 1.4 b).
- step 3 : In the T-array, the window is shifted to the right until the error is on the left side of the window. In the M-array, the window is moved until it matches with the one of the T-array (see Figure 1.4 c).
- step 4 : the windows now slides to the left and all the indices of the columns of the T-array are reset according to the two windows until another difference is detected.

	0'	1'	2'	3'	4'	5'	6'	7'	8'	9'
1'	1	0	0	1	1	1	1	1	1	1
2'	0	0	1	0	1	0	0	1	0	0
3'	0	0	0	0	1	1	1	0	0	1

T-array

	0'	1'	2'	3'	4'	5'	6'	7'	8'	9'
1'	1	0	0	1	1	1	1	1	1	1
2'	0	0	1	0	1	0	0	1	0	0
3'	0	0	0	0	1	1	1	0	0	1

T-array

	0	1	2	3	4	5	6	7	8	9	10	11
1	1	0	0	1	1	1	1	1	1	1	1	1
2	0	0	1	0	1	0	1	0	0	1	0	0
3	0	0	0	0	1	1	1	1	0	0	1	1

M-array

a

	0	1	2	3	4	5	6	7	8	9	10	11
1	1	0	0	1	1	1	1	1	1	1	1	1
2	0	0	1	0	1	0	1	0	0	1	0	0
3	0	0	0	0	1	1	1	1	1	0	0	1

M-array

b

	0'	1'	2'	3'	4'	5'	6'	7'	8'	9'
1'	1	0	0	1	1	1	1	1	1	1
2'	0	0	1	0	1	0	0	1	0	0
3'	0	0	0	0	1	1	1	0	0	1

T-array

	0'	1'	2'	3'	4'	5'	6'	7'	8'	9'
1'	1	0	0	1	1	1	1	1	1	1
2'	0	0	1	0	1	0	0	1	0	0
3'	0	0	0	0	1	1	1	0	0	1

T-array

	0	1	2	3	4	5	6	7	8	9	10	11
1	1	0	0	1	1	1	1	1	1	1	1	1
2	0	0	1	0	1	0	1	0	0	1	0	0
3	0	0	0	0	1	1	1	1	1	0	0	1

M-array

c

	0	1	2	3	4	5	6	7	8	9	10	11
1	1	0	0	1	1	1	1	1	1	1	1	1
2	0	0	1	0	1	0	1	0	0	1	0	0
3	0	0	0	0	1	1	1	1	0	0	0	1

M-array

d

Figure 1.4: Detection of the disorders

Then, as regions of the T-array extends because of the step 4, a new window can be initialized on the extended region and the growing starts again. At the end, except some array cells corresponding to dots lighted near the border of two objects, all the indices of the T-array have been determined.

Detection of Pattern Disorders

Knowing that, in the T-array, the elements which still have no indices appear to be mostly alone or draw a chain, some rules permit to correct the index of these elements.

- if the element at the top and at the bot have the same index k , the current element has also this index k .
- if the element at the left has the index $k-1$ and the one at the right $k+1$, then the current element has the index k .
- the difference between the index of two horizontal neighbors corresponding to closer positions on the image is one.
- if the indices of a consecutive vertical sequence are still undetermined, they get the index of the element at the top or bottom of the vertical.
- if the indices of an consecutive horizontal sequence are still undetermined, they get the index such as it increases by one from index determined on the left to the on the right.

k-5	k-4	k-3	k-2	k-1	k	k+1	k+2	k+3	k+4	k+5
-----	-----	-----	-----	-----	---	-----	-----	-----	-----	-----

According to [9], the previous rules should correct the most of the errors of indexation and the cases where the error cannot be corrected are scarce.

1.2.3 Grid Indexing

The method of the binary M-array projection is based on the matching of a binary array, but other patterns can be used too to permit the matching of the projected and observed patterns. A non-exhaustive list of grid indexing is presented below.

1.2.3.1 Mini-patterns Used as Code Words

Instead of using a binary array, a technique can be using a array of words coded by patterns. Each pattern codes a word. As instance, on the figure 1.5, three words has been coded and permits to convert the projected pattern into a array of integers.

1.2.3.2 2D Array of Color-coded Dots

Another technique is the 2D array of color-coded dots. The concept of this method is almost the same as the previous one but instead of using pattern to code a word, colors are used (see Figure 1.6).

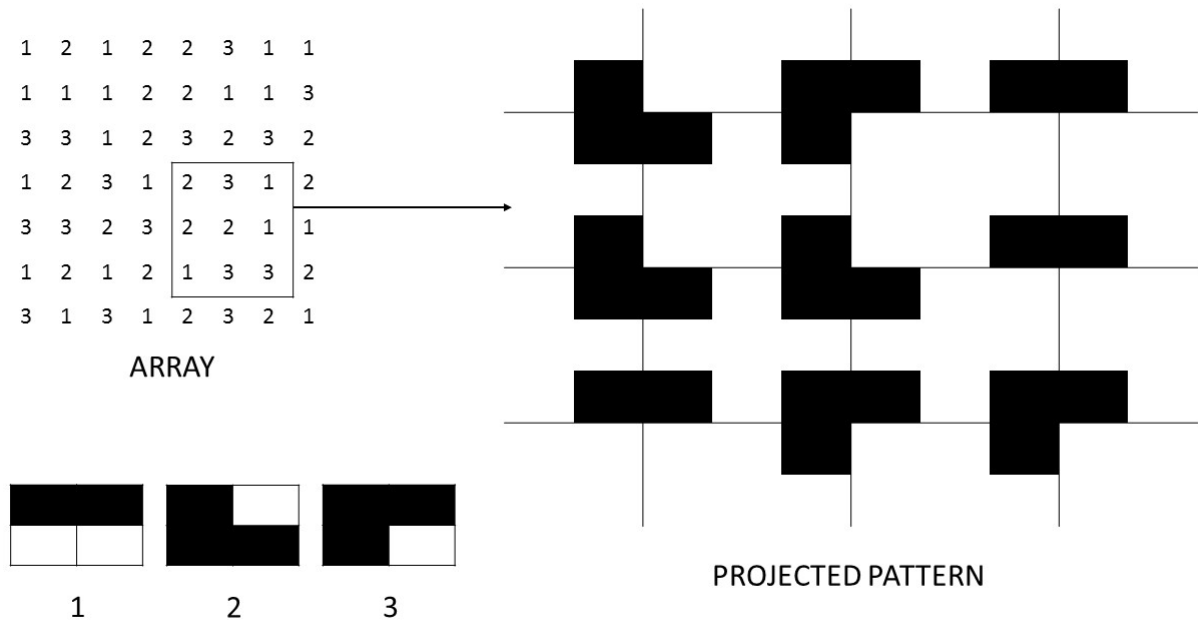


Figure 1.5: Mini-pattern used as code words

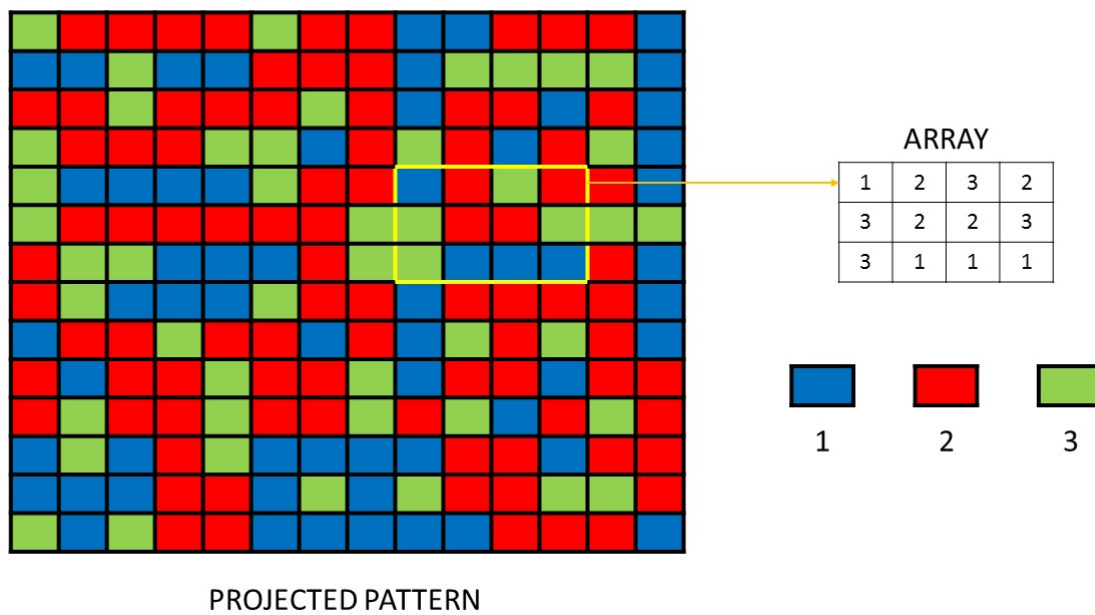


Figure 1.6: 2D Array of Color-coded Dots

1.3 Image processing

In the following part of this report, the color detection will be used to distinguish color light points sent from a luminous source from the background, the Martian rocks. In order to implement this color detection, the HSV color model needs to be defined, as well as some morphological operations.

1.3.1 HSV Color System

HSV stands for Hue Saturation Value. It is a color system which allows the separation of the color components from the intensity, unlike RGB system. It is more intuitive to find a plain object by varying HSV parameters.

The Hue designates the color itself. As it can be seen on the figure 1.7, the color is determined by an angle between 0° and 360° . Red corresponds to 0° , green to 120° and blue to 240° . OpenCV range is 0-180. Changing the Saturation will affect the intensity of the color. A low value indicates a dull color. The Value has an impact on the luminosity of the color. Decreasing this value makes the color darker. The S and V are varying between 0 and 1 but the OpenCV range is 0-255.

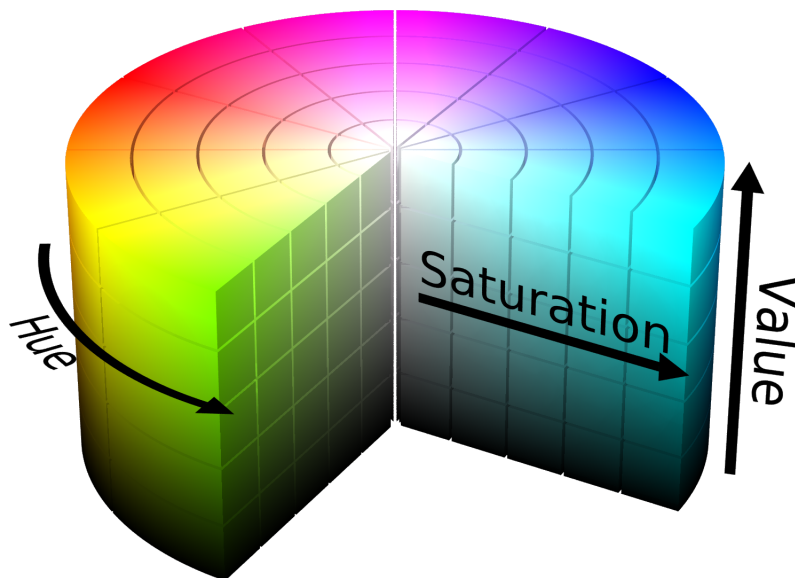


Figure 1.7: HSV diagram [14]

1.3.2 Morphological Operations [3]

The morphological operations on a binary image consists of applying a structuring element to each pixel of the object parts to reshape them. Two basic operations will be used later on and are explained here: the erosion and the dilation.

Detailed diagram of the erosion and dilation can be found below (figures 1.8 and 1.9). It should be noticed that for more legibility, the background is in white and the object in color. It will however be assumed that the pixels of the object have a value superior to the background.

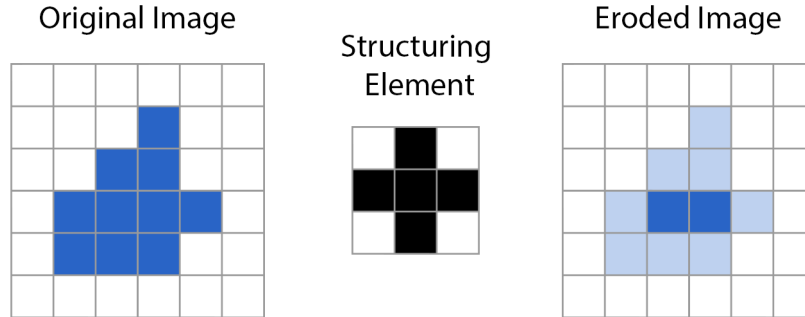


Figure 1.8: Erosion principle

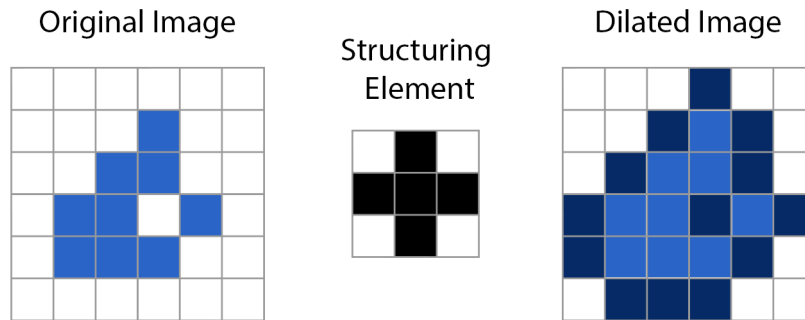


Figure 1.9: Dilation principle

1.3.2.1 Erosion

This transformation is similar to the logic gate AND. The structuring element or kernel is moved along the image and the minimal pixel value is set as the new value of the anchor point, in the figure, the center of the structuring element. This means that if all the points of the kernel are on an object (a white object on a black background), the anchor point will keep its value. On the contrary, if any element of the kernel is out of the object, the center point will become part of the background. The erosion is useful to separate two objects connected and to remove objects which are smaller than the size of the structuring element (noise).

1.3.2.2 Dilation

The dilation is the opposite transformation of the erosion. It corresponds to the OR. If one element of the kernel is on the object (which is still assumed to have the maximal value for its pixel), the anchor point will be set to this value and thus

be turned into a part of the object. This operation permits to fill holes in an object, to increase the size of an object and to link objects which are closer than the size of the structuring element.

1.3.2.3 Opening

When combined, first by operating an erosion and then a dilation, the transformation is called an opening. The inverse operation is the closing. An opening could be convenient to separate luminous points which are connected and to then increase their size, lessen by the erosion.

Part 2

Development

2.1 Scene Analysis

2.1.1 Camera

In order to design the camera and find its characteristics, a scene analysis have to be carried out. Our study is based on the MER (Mars Exploration Rover) cameras properties [8]. To begin with, we choose an image sensor.

2.1.1.1 CCD

The Charge Coupled Device (CCD) is commonly more sensitive to light than its counterpart, the CMOS (Complementary Metal Oxide Semiconductor). Moreover, in the near infrared CCD appears to have a better response. Since Mars has a reddish color, it seems more accurate to select the CCD detector.

As scientists will need to discern the details of rocks, the resolution should be around the megapixel. Taking into account the cost, which will increase with the resolution, and the time of computation for an image with too many pixels, 1024×1024 seems to be an acceptable compromise.

Finally, the last element to consider is the pixel size. A trade-off have to be found between having a higher resolution (smaller pixels) and more sensitivity (larger pixels). All the camera of the MER mission were conceived with a pixel size of $12 \times 12 \mu m^2$ for a resolution of 1024×1024 . It was decided to comply with that value.

For the next parts of this report, we will use the data sheet of the FTT1010M CCD image sensor (see Appendix B) as a basis for our calculations which will require CCD details.

2.1.1.2 Field of View

According to the book [5], the Field of View (FoV) “is the angle of the cone of directions encompassed by the scene that is being images”. This solid angle is needed to compute the focal length the camera should have.

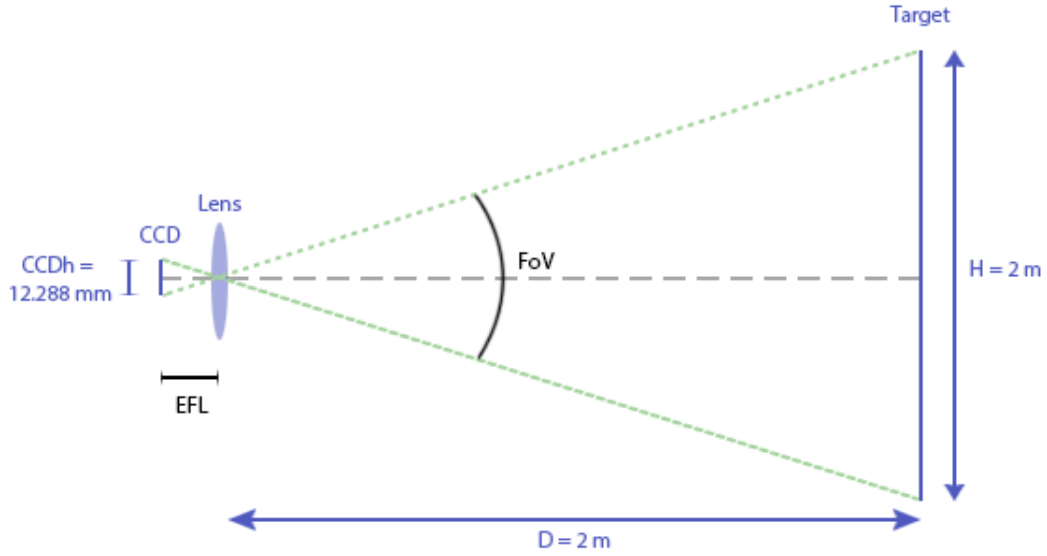


Figure 2.1: Field of View and Effective Focal Length

A simple relationship between the distance lens-target, the size of the target and the FoV can be deduced from the detailed diagram 2.1:

$$\tan\left(\frac{FoV}{2}\right) = \frac{1}{2} \times \frac{H}{D}$$

We derive and get

$$\frac{FoV}{2} = \text{atan}\left(\frac{1}{2} \times \frac{H}{D}\right)$$

Numerically, with our problem delimitation, the Field of View is equal to $26.6^\circ \times 26.6^\circ$.

2.1.1.3 Focal Length

Thanks to the previous diagram, the Effective Focal Length (EFL) can also be determined:

$$EFL = \frac{1}{2} \times \frac{CCDh}{\tan\left(\frac{FoV}{2}\right)} = 12.29 \text{ mm}$$

where $CCDh$ is the image section of the CCD according to the data sheet.

In order to get the real focal length, we choose $rf = 1\text{ m}$ for the distance of focus of the camera.

$$f = \frac{1}{\frac{1}{rf} + \frac{1}{EFL}} = 12.14\text{ mm}$$

2.1.1.4 Aperture

To determine the diameter of the aperture, several criteria have to be accounted for. If the diameter is too small, the sharpness of the image will decrease due to the diffraction effect. In fact, at large aperture, the diffracted light is negligible compared to the total amount of light entering the system. On the other hand, we should also consider the Depth of Field (FoV). We need to insure that it is big enough to allow us to see the whole target on the image. The relationship between the DoF and the diameter is inversely proportional. That means that if we increase the diameter, we will lessen it. The Diameter of Confusion (DoC), linked to the DoF is also a factor to take into consideration for the choice of the diameter. According to Wikipedia [13] It corresponds to “an optical spot caused by a cone of light rays from a lens not coming to a perfect focus when imaging a point source”. The smaller the DoC is, which corresponds to a better focus, the bigger is the DoF, and also the smaller is the diameter.

As the behaviour of the depth of field and of the diameter of confusion runs counter to the diffraction one, a trade-off has to be found.

These formula are used to calculate the diameter of confusion and the diffraction spot:

$$DoC = Dsr \cdot \frac{|r - rf|}{r} \cdot \frac{f}{rf - f}$$

where Dsr is the diameter of the aperture

$$DiffractionSpot = 2 \cdot EFL \cdot \tan(1.22 \cdot \frac{\lambda}{Dsr})$$

where λ is a wavelength of the sunlight

In the delimitations, it is assumed that the wavelengths of the sunlight belong to [400 800] nm. To settle on a diameter, the diameter of confusion and the diffraction spot were computed for diameters varying from 1 mm to 5 mm and wavelengths from 400 nm to 800 nm. The results are shown graphically in figure 2.2. As the diameter of confusion cannot be bigger than the height of a pixel, the line corresponding to $12\text{ }\mu\text{m}$ was also added to the graphic. In order to have the

best trade-off, that is to say all the curves under $12\ \mu m$, we have chosen a effective lens entrance aperture D_{sr} equal to $1.9\ mm$, corresponding to $DoC = 0.0117\ mm$.

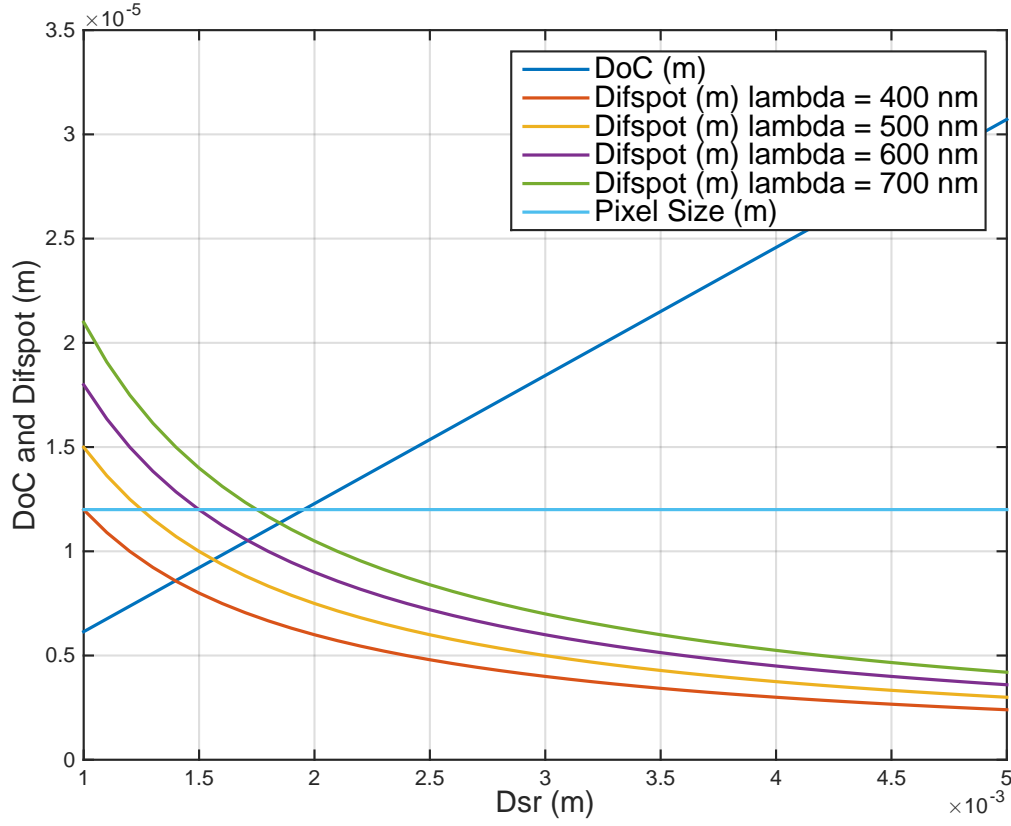


Figure 2.2: Diameter of confusion and diffraction spots as a function of the diameter

Then, the depth of field can be deduced:

$$DoF = \frac{2 \frac{f}{D_{sr}} DoC (m+1)}{m^2 - \left(\frac{DoC}{D_{sr}}\right)^2} = 1.33\ m$$

That means that the roughness of the rock analysed cannot be more than $\frac{DoF}{2} = 66.5\ cm$ since we could not see the whole rock if not, and the 3D map will then be flawed.

2.1.2 Artificial Light Source

In order to carry out a 3D mapping of the target, the system needs a light source to project points which will be used by the 3D mapping algorithm. In this section, the source of light will be designed.

2.1.2.1 Design of the Light Source

First of all, the green has been chosen as color of the light source. Indeed, in order to detect easily the points projected on the target, a distinctive color should be used. As we can see figure 2.3, the CCD selected for the camera has the best quantum efficiency for a wavelength around 510 nm , which means that the green is the color that is the best recorded by the camera. Secondly, as the surface on Mars is mainly orange, red and brown, this color should stand out.

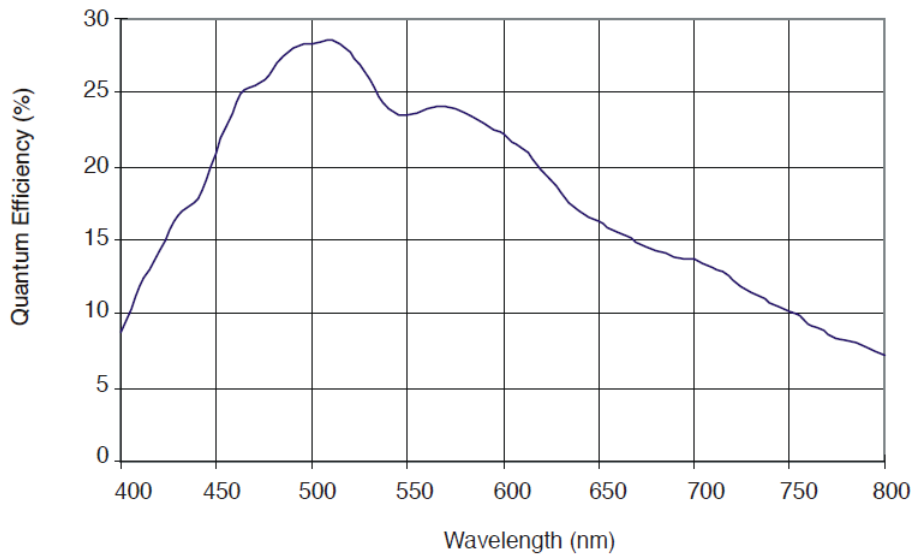


Figure 2.3: Quantum efficiency versus wavelength of the CCD

Then, as only 300 mW are available to aliment the light source and a lot of lightning energy is needed to outshine the sunlight, a LED has been chosen. Indeed, LEDs have great energy performances. The properties of the chosen LED can be seen in Annex A. Note that the use of a laser have been studied, but the energy cost would have been too expensive. Moreover, even if we cannot obtained a coherent light, as a laser do, with a LED, it is still feasible to obtain a monochromatic and directional light. Thus, we will assume that the LED can bring enough light (proof in part on Signal Noise Ratio 2.1.2.2). Then, as the 3D mapping algorithm needs a grid of points, the LED cannot be used in its present condition. Moreover, lot of light would be lost without an optic system. Thus, a system has been designed to concentrate the luminous beams of the LED and to transform the continuous light into a grid of point. The system uses a lens and a grid (Figure 2.4).

As the LED has a diffusion angle of 30° (Annex A), the lens needs to be close enough to collect all the light beams of the LED to avoid losses of energy. In order

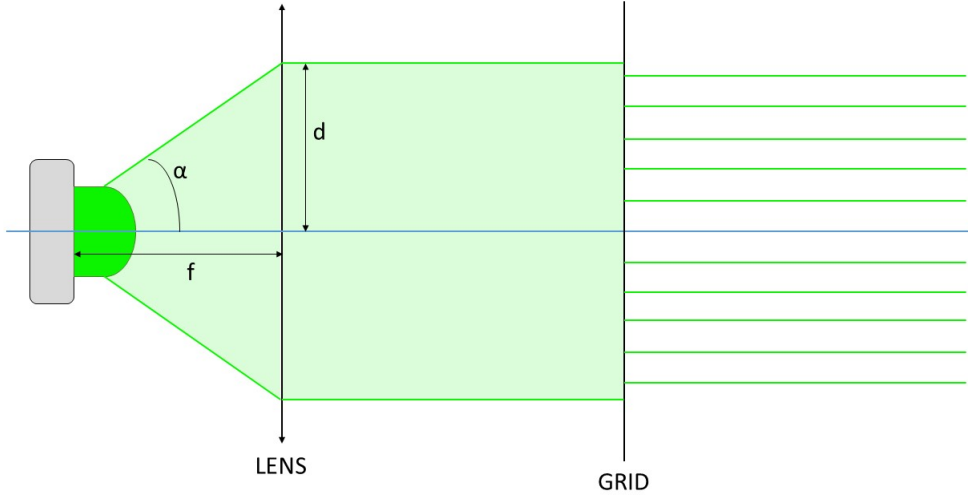


Figure 2.4: schema of the LED system

to capture as much light as possible, the diameter of the lens should follow (2.1).

$$d = f \tan \alpha \quad (2.1)$$

with

$$\alpha = \frac{30}{2} = 15^\circ, \text{ the half of the diffusion angle.}$$

f , the focal length of the lens

Moreover, it should be pointed that there is a loss of energy because of the lens and the grid. We will assume that the energy loss coefficient of the lens LFL_{led} (Loss Factor Lens Led) is 0.5 and the one of the grid LFG_{led} (Loss Factor Grid Led) is 0.3.

2.1.2.2 Validation of the Light Source

In order to verify whether our light source has enough power or not to outshine the sunlight, the Signal/Noise ratio (SNR) has to be calculated (see part Signal/Noise ratio 2.1.3.5). Knowing that 100 is a really great SNR, as the SNR of images recorded with this system is [32, 348], it can be concluded that the LED can be chosen as light source. Indeed, even if 32 is a low ratio, it is only when all the different poor conditions happen in the same time and it does not happen frequently. Moreover, 100 to 347 are really high ratios that permit to have the 3D

algorithm working well. Thus, the design of the light source is validated.

2.1.3 Signal Noise Ratio

2.1.3.1 Irradiance

First of all, the irradiance F of the light from the sun falling at the top of the atmosphere of Mars can be calculated as following : Conservation of energy :

$$4\pi R_{\odot}^2 F_{\odot} = 4\pi R^2 F \quad (2.2)$$

with

$$R_{\odot} = 6,956.10^8 \text{ m} : \text{solar radius}$$

$$F_{\odot} = 6,45.10^7 \text{ W.m}^{-2} : \text{energy flow of the surface of the sun}$$

$$R \in [2.06644, 2.49228].10^{11} \text{ m} : \text{distance Mars-Sun (Aphelion and Perihelion)}$$

$$F = F_{\odot} \left(\frac{R_{\odot}}{R} \right)^2 \in [502, 730] \text{ W/m}^2 \quad (2.3)$$

In this report, we will consider that the rover is working on a specific date and we will chose the one when R corresponds to the semi-major axis. In this case $R = 2,27936.10^{11} \text{ km}$ and

$$F = 589 \text{ W/m}^2 \quad (2.4)$$

Moreover, we can assume that a part of the irradiance is absorbed by the atmosphere. Knowing that the atmosphere of Earth absorbs and scatters to space around 30% of the incident irradiance of the Sun[15], and knowing that the atmosphere of Mars is thinner than the one of the Earth (150 times less dense), we will postulate that 10% of the incident irradiance is absorbed. Thus, using (2.4) the actual irradiance F_a of the light from the sun falling on the surface of Mars is

$$F_a = \frac{90}{100} F = \frac{90 * 589}{100} = 530 \text{ W/m}^2 \quad (2.5)$$

However, this irradiance is the one of surface exposed perpendicular to the sun's beams. As Mars is a sphere, the projection need to be considered. Knowing that the weather is better into the northern hemisphere of Mars (1.1.2) and the fact that a latitude between 30 and 70 degrees is favored for a landing[6], we will assume that the rover has a latitude of 50° . This latitude corresponds to an angle

of 40° between the surface of Mars and the sun's beams. Moreover, suppose that the rover stop working when this angle is inferior to 10° . Thus, the irradiance F_{50} at a latitude of 50° is

$$F_{50} = F_a \sin(\text{angleBeams}) \in [92, 341] \text{ W/m}^2 \quad (2.6)$$

with $\text{angleBeams} = [10, 90 - \text{latitude}] = [10, 40]^\circ$.

2.1.3.2 Target's Radiance

Considering the trajectory of the Sun into the sky of Mars and knowing that the rock target is more or less vertical to the surface of Mars, the angle θ between the target's normal and the sun's beam is considered to be included in $[10, 50]^\circ$. In addition, in the optimal case (when all the optimal conditions are provided to have the maximal radiance), the BRDF of the surface of the target is assumed to be 90% Lambertian and 10% Glossy while in the worst case the BRDF will be only Lambertian. In this way, the radiance of the target R_T is

$$R_T = \begin{cases} \frac{F_{50}\alpha}{\pi} \cos \theta & \text{optimal case} \\ F_{50}\alpha \left(\frac{9}{10\pi} \cos \theta + \frac{1}{10} \right) & \text{worst case} \end{cases} \quad (2.7)$$

with

$\alpha \in [0.05, 0.45]$, the albedo of the target

$\theta \in [10, 50]^\circ$, the angle between the target's normal and the sun's beam

Thus,

$$R_T \in [1.44, 58.58] \text{ W/m}^2 \quad (2.8)$$

2.1.3.3 Target's Irradiance

Now, the irradiance of the target I_T can be calculated with

$$I_T = R_T \frac{\pi}{4} \left(\frac{Dsr}{EFL} \right)^2 \cos(\alpha_{CT})^4 \quad (2.9)$$

with

α_{CT} the angle between the normal of the target and the axis of the camera

Dsr the effective lens entrance aperture

EFL the focal length

However, knowing that the camera is supposed to be right in front of the target, we have

$$\alpha_{CT} = 0$$

And according to (2.9), (2.8), 2.1.1.4 and 2.1.1.3, we have

$$I_T \in [0.0271, 1.1000] \text{ W/m}^2 \quad (2.10)$$

Finally, the luminous power from the target to the camera per pixel W_{lum} is

$$W_{lum} = I_T P_s \quad (2.11)$$

with

$$P_s = 12.10^{-6} \times 12.10^{-6} \text{ m}^2, \text{ the pixel size of the CCD}$$

According to (2.10)

$$W_{lum} \in [3.900, 158.40].10^{-10} \text{ W/pixel} \quad (2.12)$$

2.1.3.4 Light Source Irradiance

Now, the luminous power of the light toward the CCD from the light source reflected by the target W_{LED} needs to be determined. First, the luminous power of each point W_{dot} projected by the source is

$$W_{dot} = \frac{LFLLed.LFGLed.P_{LED}}{N_{point}} = 4,4960.10^{-04} \text{ W} \quad (2.13)$$

with

$N_{points} = 10 \times 10 = 100$ points, the number of points projected on the target

$P_{LED} = \frac{C_{LED}\Omega}{L_e} = 0.2997$ W, the power of the LED

$C_{LED} = 84$ cd, the power of the LED in candella (Annex A)

$\Omega = 2\pi(1 - \cos \alpha) = 0.2141$ sr, the solid angle of the LED (Annex A)

$L_e = 60$, the luminous efficiency of the LED

Then, the irradiance of a light point E_{point} is

$$E_{point} = \frac{W_{dot}}{A_{point}} = 71.5558 \text{ W/m}^2 \quad (2.14)$$

with $A_{point} = 6,2832 \cdot 10^{-6} \text{ m}^2$, the surface of a point.

Finally, W_{LED} can be calculated following the same steps as in the previous part 2.1.3.3 except the fact that we have to consider an angle $\theta_{Led} = 10^\circ$ between the light source and the normal of the target. Thus, the luminous power per pixel received by the CCD from the source light is $W_{LED} = [3.033, 33.271] \cdot 10^{-12} \text{ W/pixe}$

2.1.3.5 Signal/Noise Ratio

Three different cases will be studied. In the first one, we examine the case of a target illuminated by the sun without the use of laser, the second one considers the use of lasers by night and the last one, which is the case that we need to consider for our rover, study the use of lasers by daylight. In order to calculate the Signal/Noise ratio, the different noises need to be determined. Three will be taken into account: the readout noise, the dark current noise and the noise from the sun light.

The three different cases have the readout and the dark current noise in common which are given by the datasheet of the CCD B.

$$\delta_{readout} = \frac{RMS}{N_{pixel}} \quad (2.15)$$

$$= 2,3842.10^{-05} \text{ el/pixel} \quad (2.16)$$

$$\delta_{dark} = \left(2,55.10^{15} N_{dc0} T_s (P_s.10^2)^2 T^{\frac{2}{3}} e^{-\frac{E_g}{2kT}} \right)^{\frac{1}{2}} \quad (2.17)$$

$$= 0.0067 \text{ el/pixel} \quad (2.18)$$

with

$RMS = 25 \text{ el}$, the RMS readout noise B

$N_{pixel} = 1024 \times 1024 \text{ pixels}$, the number of pixel of the CCDB

$N_{dc0} = 30 \text{ pA/cm}^2$, the dark current level at 20°C B

$T_s = 0.1 \text{ s}$, the shutter time

$P_s = 12.10^{-6} \text{ m}$, the pixel size B

$T = 197 \text{ K}$, the temperature

$$E_g = 1.1557 - \frac{7.10^{-4} T^2}{1108 + T}$$

$k = 8,62.10^{-5} \text{ eV/K}$, the Boltzmann's constant

First case

In this case, the signal that needs to be considered is the sun light reflected by the target. Therefore, the readout and the dark current noises are the only two which need to be considered and the noise is

$$N = \sqrt{\delta_{readout}^2 + \delta_{dark}^2} = 0.0067 \text{ el/pixel} \quad (2.19)$$

Then, the number of photons per shutter time N_p corresponding o the radiance of the target is

$$N_p = \frac{1}{\lambda_{max} - \lambda_{min}} \int_{\lambda_{min}}^{\lambda_{max}} \frac{W_{lum} ts}{\frac{h.c}{\lambda}} d\lambda \in [1.177, 47.810].10^6 \text{ photons/pixel} \quad (2.20)$$

with

$ts = 0.1$ s, shutter time

$h = 6,6263.10^{-34}$ J.s, Planck's constant

$c = 3.10^8$ m/s, velocity of light

$\lambda \in [400, 800]$ nm, wavelength of the sunlight

The number of photons per pixel going to the lens N_{CCD} is

$$N_{CCD} = \frac{\pi \left(\frac{D_{sr}}{2}\right)^2}{2\pi(r)^2} N_p \in [0.1328, 5.3936] \text{ photons/pixel} \quad (2.21)$$

with $r = 2$ m, the distance between the camera and the target

The number of photons per pixel to the lens registered by the CCD Nen_{CCD} is

$$Nen_{CCD} = N_{CCD} \int_{\lambda_{min}}^{\lambda_{max}} CCDqe(\lambda).alphaLens(\lambda) d\lambda \in [0.0208, 0.8457] \text{ photons/pixel} \quad (2.22)$$

with

$CCDqe$, the quantum efficiency of the CCD 2.3

$alphaLens$, the pass band efficiency of the lens

Finally, according to (2.19) and (2.22) we obtain the Signal/Noise ratio

$$\frac{S}{N} = \frac{Nen_{CCD}}{N} = [3.1, 126.8] \quad (2.23)$$

Knowing that, 100 is a really great Signal/Noise ratio, we can conclude that the system could record images of satisfactory or high quality the most of the time. However, if the different poor conditions accumulate, the quality of the image will greatly decrease.

Second case

In this case, the signal that needs to be considered is the light of the pseudo laser reflected by the target. Therefore, the noise is still the same as in the first case. Proceeding in the same way as into the first case 2.1.3.5 but considering only the wave

length of the LED ($520.10^{-9} m$), the number of photons per pixel from the artificial light source going toward the CCD is $Nen_{LED} = [2.4556, 26.9410] \text{ photon/pixel}$.

And the Signal/Noise ratio is given by

$$\frac{S}{N} = \frac{Nen_{LED}}{N} = [368, 4040] \quad (2.24)$$

It can be deduced from this SNR that the system light source plus camera would work perfectly by night. Indeed, the minimum of this ratio is 368 which is larger than 100, an excellent ratio. Working by night would be the best scenario but the day work needs to be considered.

Third case

In this case, the current case, it will be determined if the artificial light source is powerful enough to outshine the sunlight. Thus, the sunlight is now considered as a noise, the shot noise.

$$N = \sqrt{\delta_{readout}^2 + \delta_{dark}^2 + \delta_{shot}^2} = [0.0219, 0.8457] \text{ el/pixel} \quad \text{with } \delta_{shot} = nen_{CCD} \quad (2.25)$$

As the signal and the noise are ranges because of the different conditions possible, the SNR should be

$$SNR = \left[\frac{S_{min}}{N_{max}}, \frac{S_{max}}{N_{min}} \right] \quad \text{with } S = Nen_{LED}$$

However, it can be noticed that one parameter, the albedo α , is varying for both lights, the sun and the artificial light source. Indeed, if the target has an albedo α_{min} , this albedo needs to be considered in both calculation of the Nen_{CCD} and Nen_{LED} . Therefore, the calculation of the SNR needs to take into account this correlation and we have

$$SNR = [32, 348] \quad (2.26)$$

It can be concluded that the artificial light system is powerful enough to outshine the sunlight. Moreover, the quality of the image of the points should have an excellent quality, which would permit the 3D mapping algorithm to work perfectly. Also, even if the worst conditions are gathered (minimum albedo, sunset), the SNR is still equal to 32, which is acceptable.

2.1.4 Summary and Comparison with MER Cameras

To validate the coherence of the characteristics of the designed camera, a comparative table 2.1 with the MER cameras Navcam (Navigation Camera) and Pancam (Panoramic Camera) [8] can be found below.

Table 2.1: Recap chart of the Designed Camera and Comparison with Navcam and Pancam (MER Cameras)

Features	Designed Camera	Navcam	Pancam
CCD			
Pixel size	12×12 microns	12×12 microns	12×12 microns
Resolution	1024×1024	1024×1024	1024×1024
Spectral range	[400 - 800] nm	[600 - 800] nm	[400 - 1100] nm
Readout noise, 55°	25 electrons	25 electrons	25 electrons
Optical properties			
Focal length	12.14 mm	14.67 mm	43 mm
Entrance pupil diameter	1.9 mm	1.25 mm	2.18 mm
FOV	$26.6^\circ \times 26.6^\circ$	$45^\circ \times 45^\circ$	$16^\circ \times 16^\circ$
Depth of field	0.67 - 2 m	0.5 m - infinity	1.5 m - infinity
Best focus	1 m	1 m	3 m

The CCD parameters are similar except for the spectral range. As Pancam mission is to investigate Mars terrain and obtain color images of any information useful to learn more about the Red Planet, that seems logical that the spectrum is wider than the one we choose. The navigation camera provides a 360° view of the area where is located the rover. The spectrum was reduced using filters to allow a higher spectral responsivity. For the optical features, it can be noticed that the parameters have approximately the same size. The depth of field for our camera is restricted but it is due to our aim: stabilising the camera in front of a rock and carrying out its depth map. We can conclude that since the MER cameras accomplish well their task, the designed camera which is comparable to them should also be capable of acquiring good images on Mars.

2.2 Distance Camera-Target of One Point

Before starting to establish a whole 3D mapping, a more simple case can be studied first and it will be shown, in this section, how to determine the distance to

only one point. Indeed, the distance between the camera and a point of the target can be easily determined thanks to a little bit of trigonometry.

The context of this case is simple, the camera is recording images of the target while the artificial light source is projecting a point on the last one (see figure 2.5).

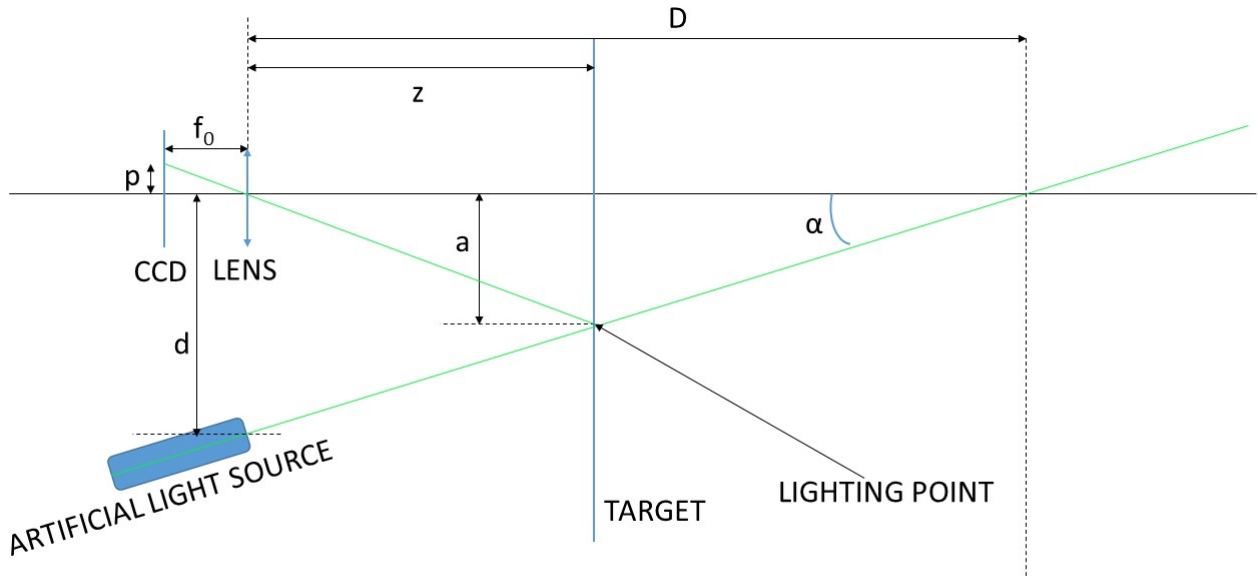


Figure 2.5: schema of the camera recording images of the target on which there is a lighting point from the artificial light source

According to the figure 2.5,

- z is the distance to determine.
- α is the angle between the focal axis of the camera and the focal axis of the light source.
- a is the distance between the focal axis of the camera and the lighting point.
- D is the distance between the camera and the lighting point when this one is on the focal axis of the camera.
- d is the distance between the camera and the light source
- p is the distance between the focal axis and the image of the lighting point on the CCD

Thus, we have

$$d = D - \frac{a}{\tan \alpha}$$

However, α , a and D are not known yet, that is why a calibration phase is needed (see Figure 2.6). The first parameter, α , is determined during the installation of the light source and the camera on the rover. Then, during the calibration, two steps can be identified. During the first one, a target is positioned such as the lighting point is on the center of the image recorded by the camera. Thus, D can be measured. During the second step, a target is positioned such as the lighting point is right on side (left or right) of the image recorded by the camera (see Figure 2.6). Therefore, a_0 can be measured and we have

$$\frac{a_0}{p_0} = \frac{z_0}{f_0} \quad \text{and} \quad \frac{a}{p} = \frac{z}{f_0}$$

Thus, we have

$$a = \frac{pza_0}{p_0z_0}$$

And finally,

$$z = \frac{Dp_0z_0 \tan \alpha}{p_0z_0 \tan \alpha + pa_0}$$

The distance p and p_0 can be determined using the pixel size P_{size} such as

$$p = P_{pixels}P_{size}$$

but the pixel size P_{size} can be simplified and the final formula is

$$z = \frac{Dp_{pixels_0}z_0 \tan \alpha}{p_{pixels_0}z_0 \tan \alpha + p_{pixels}a_0}$$

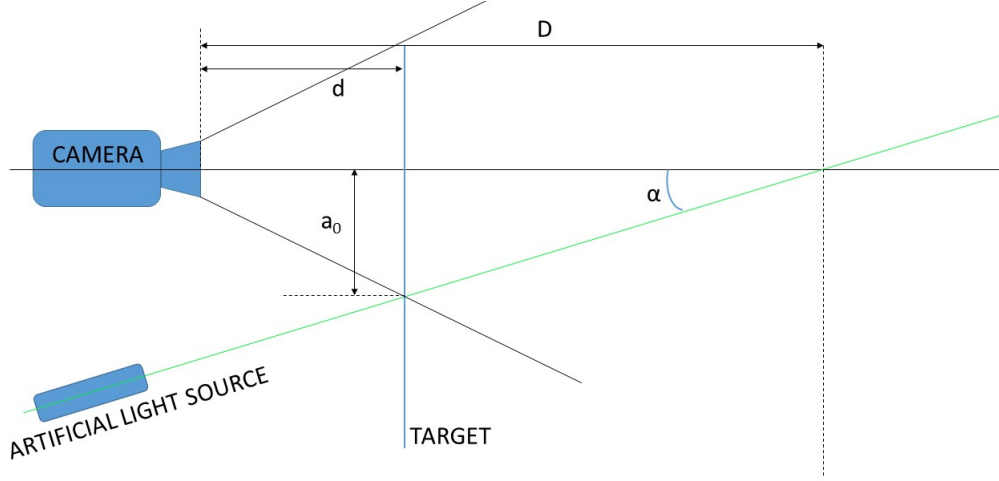


Figure 2.6: schema of the calibration

However, a calculation of the distance camera - target using a simpler calibration can be found thanks to triangulation. Indeed, using the Thales' theorem such as $\frac{z}{f_0} = \frac{a}{p}$ (see Figure 2.5), it can be determined that the distance z camera - point on the target is

$$z = \frac{f_0 d}{p + f_0 \tan \alpha}$$

Thus, only the first step of the calibration is needed because only α and d need to be determined. f_0 is a characteristic of the lens and p is determined thanks to the CCD characteristics ($p = p_{pixels} P_{size}$).

$$z = \frac{d}{p_{pixels} \frac{P_{size}}{f_0} + \tan \alpha} \quad (2.27)$$

2.3 Image Processing

To carry out the 3D map of a Martian rock, the coordinates of the points which are projected by the LED on its surface need to be determined on the images acquired by the camera. They are obtained by detecting the points thanks to their color, by distinguishing them, and by applying the centroid algorithm to get their center. First, the color detection method will be addressed, before focusing on the differentiation and the centroiding.

2.3.1 Color Detection

To increase the robustness of the algorithm, the color of the light beams was chosen to have the maximum contrast with the color of the rock. Mars having a reddish color, a bright green light seemed adapted. Moreover, as it is explained in the scene analysis part, the CCD sensor is more sensitive to the wavelength corresponding to the green (around 520 nm). Thus, the color detection algorithm aims to find bright green spots in the camera video stream in real time. It is implemented in C with OpenCV library.

For unit testing, the image analysis is performed by extracting frames from the video stream obtained thanks to the computer webcam. These images are processed very quickly, which allows a real time analysis. The details of the method employed are given below. For the explanation, the figures are obtained for the detection of a blue box (the H value was changed for this purpose), but the algorithm works similarly for green light beams.

To begin with, a low-pass filter is applied to the image to handle to smooth it and to reduce the noise. Once achieved, the image is converted from RGB to HSV (see Theory Section) in order to get a better control of the colors and intensities of the image pixels. The range of the HSV parameters can be determined to isolate the bright green pixels from the rest of the image. The equivalent hue is between 60° and 180° , taking a large scope to be sure to isolate the good color component. As the luminous points will be bright, the range of the saturation and the luminosity should be chosen around the upper values. To adjust the values, several trackbars are added to the image, see figure 2.7 and the modifications are made in real time. All the values under the thresholds defined are irrelevant. Thus the pixels of the binary image which corresponds to the HSV thresholding are set to 1 (white) for the zone where the light green points are recognized and to 0 (black) for the background, the rest of the image. This image is then easier to deal with because it is only composed of two values, black and white. Erosions and dilations can be applied respectively to separate connected light beams and remove noise or to fill holes in the points. The number of erosions and dilations are selected thanks to trackbars once again (figure 2.7) and they are computed with the OpenCV functions with a 3x3 rectangular structuring element. The size of the kernel of the low-pass filter is also controllable with the trackbars.

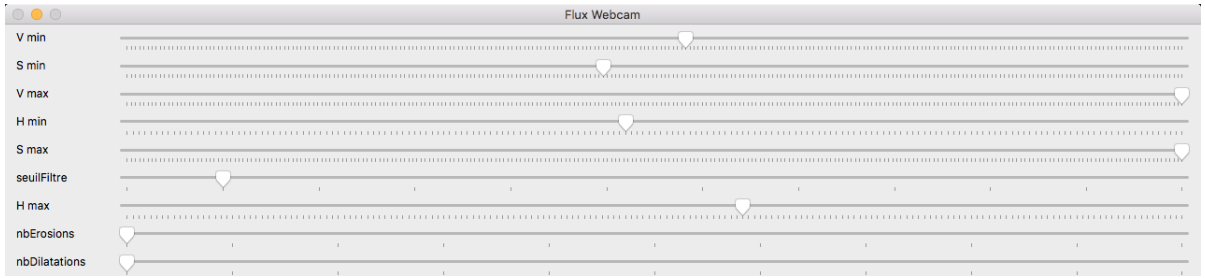


Figure 2.7: Trackbars for the threshold of the filter, the HSV parameters and the number of erosion and dilation

The calibration is carried out through the trackbars and the result is displayed on the video stream with the addition of contours to facilitate the tuning (figure 2.8). *cvFindContours* is used to search the contour of the light spots. The detection is based on the same principle that it has been seen during the exercises in the lab. The algorithm looks for the first pixel belonging to the point and then follows the contour pixel by pixel. Once the threshold of the low-pass filter, the HSV values and the number of erosion and dilation are established, the calibration is completed. For the unit testing with the blue box, we will only focus on the color detection and the centroiding. Thus, no erosion nor dilation will be added and the filter kernel is set to one pixel, which does nothing.

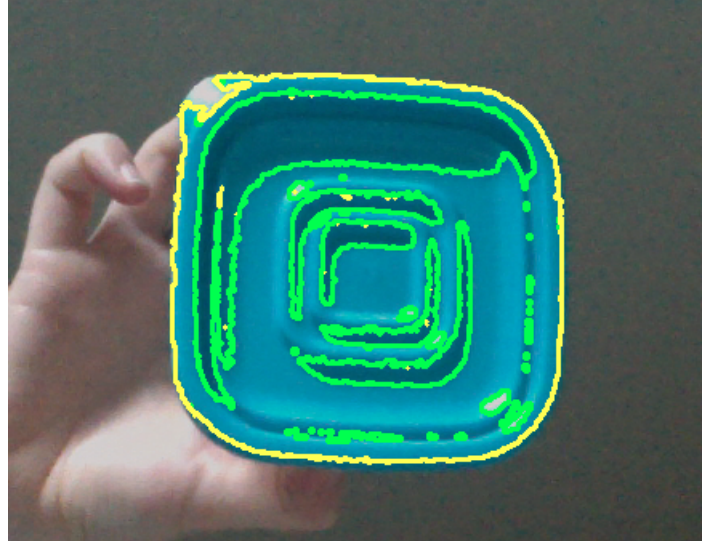


Figure 2.8: Contours of the detected object

In order to compute the centroid of the beams spots, it is needed to retrieve their intensity. To this end, the color detection should return an image with the light points in HSV color on a black background. To do so, the binary image is multiplied by the HSV image. The multiplication is explained by the pseudo code below.

```
function MULTIPLICATION(binary image, color image)
```

```

for each pixel in the binary image do
  if the pixel value is white then
     $pixelHSVColor \leftarrow$  the color of the pixel in the HSV image
    the color of the pixel in the final image  $\leftarrow pixelHSVColor$ 
  else
    the color of the pixel in the final image  $\leftarrow$  black color
  end if
end for
end function

```

The final image obtained is shown figure 2.9. Each white pixel corresponding to 1 in the binary image is replaced in the final image by the HSV value of the original image and the background is set to black like in the binary image.



Figure 2.9: Object detected in HSV color system on a black background

2.3.2 Beams Distinction

In the previous part, a unit test was performed with a blue box to check the efficiency of the color detection algorithm. However, the aim is to project a grid of 10 x 10 green points on a rock. Once they are extracted from the rest of the image with the same technique described above, they need to be separated. Indeed, for now, we only have the coordinates of the pixels assumed to belong to the beam spots. To look for their center of mass, the pixels which constitute each point have to be gathered.

It should be noticed that, as no pattern other than an unicolour grid is used to carry out the depth mapping, the green points cannot be distinguished from each others. Thus, this implementation does not take into account the position of each beam spot, which could be problematic if the deformation is too important. Indeed, if a point is slightly linked to another or if it has moved and is a bit above or under the others, it is still possible to retrieve its original position. It is only if the change is too important that it will be very complicated to get the correct location of each beam spot. To solve this problem, different patterns as described in the Structured Light Theory Section have to be projected on the rock, which would assure that no spot has been switched. Nevertheless, this method requires more material, power consumption and is dismissed in a first approach.

To differentiate each point, a recursive method was implemented using C++ which consists to isolate a point using neighbouring pixels. The pseudo code explaining the technique can be found below:

```
function FINDPOINTREC(table, pixel, information to scan the image)
  ▷ table contains the coordinates of the pixel belonging to the current point
  if the pixel value is is not black then
    add to table the pixel coordinates and its value
    the pixel value in the image  $\leftarrow$  0
    findPointRec(table, left neighbouring pixel, image information)
    findPointRec(table, right neighbouring pixel, image information)
    findPointRec(table, above neighbouring pixel, image information)
    findPointRec(table, below neighbouring pixel, image information))
  end if
end function
```

The image is scanned and it is assumed that a new point begins each time that a green pixel is detected. A table to collect the coordinates of pixels belonging to the new beam spot is created and given in parameter to the recursive method. The first pixel position is added to the table, its value is set to 0 in the image and the recursive method is repeated while neighbouring pixels are found. At the end, a 2D table is obtained where the rows correspond to the spots and the columns to each pixel belonging to the point. The centroiding algorithm can then be processed to determine the center of mass of each spot and compute their distance to the camera. We can note that, for now, the points are separated but if they were not perfectly aligned on the projection, the rows of the 2D table are not in the same order than the original projected points.

2.3.3 Centroiding

The 3D map can be performed with the coordinates of the light points seen by the camera. They are determined by estimating the centre of the spots, and to do so, the centres of mass, also called the centroids need to be calculated in the final image acquired by the color detection. In order to get it, a barycentre of the pixels belonging to the beam spot is carried out weighted by the intensity of the pixel (S value in HSV model).

$$x_c = \frac{\sum_x x \cdot I(x, y)}{\sum_x \sum_y I(x, y)} \quad (2.28)$$

$$y_c = \frac{\sum_y y \cdot I(x, y)}{\sum_x \sum_y I(x, y)} \quad (2.29)$$

Where x_c and y_c are the coordinates of the centre of mass of the spot, x and y the coordinates of each pixel belonging to the spot and I their corresponding intensity.

The intensity of each pixel is obtained by splitting the canals of the image into three to retrieve an image with only the Saturation values. Then the formulas (2.28) and (2.29) are computed. A white cross is displayed on the centroid in real time as it can be seen on the figure 2.9 or below figure 2.10(b) on a simple grid image 2.10(a).

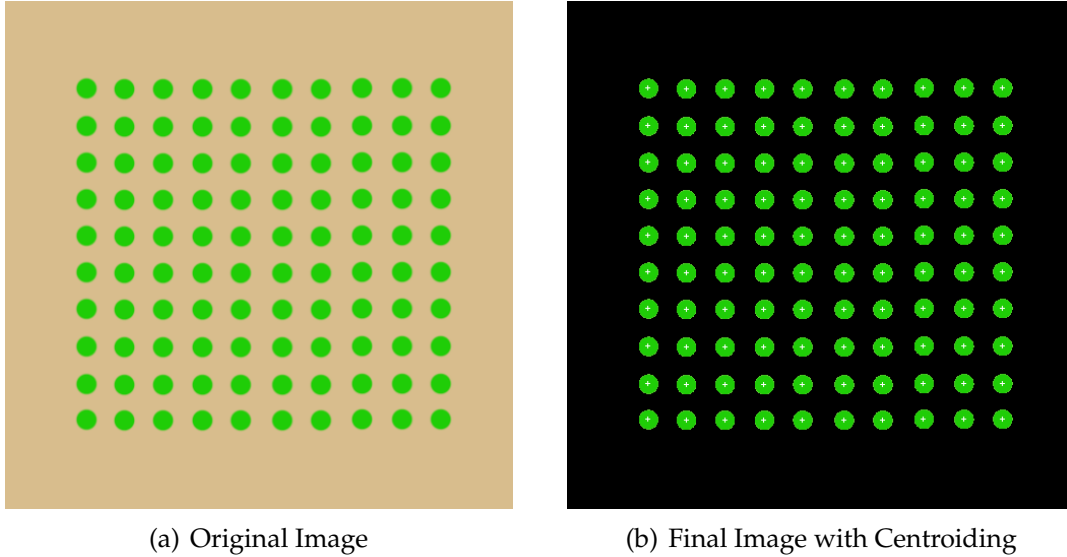


Figure 2.10: RGB images of a grid of 10 x 10 green points without any noise

In a real application, the grid will not be so perfect after the projection on the rock. Small light spots could be detected as false positive, two points could be slightly linked or some spots could be displaced. In order to deal with these

issues, three solutions are implemented:

- During the separation step, if a point has an insignificant number of pixel, it is dismissed. The threshold can be adjusted knowing the expected size of a point.
- Morphological operations (see Theory Section) such as openings are used to disconnect two linked points. The number of erosion and dilation to carry out to separate the points without losing too much information about the points have to be calibrated.
- A bubble sort of the x (or horizontal) coordinate of the centroids is implemented. It consists of finding the maximum x between two consecutive centres of mass and swap them if the bigger value is before the lower. The algorithm goes once through the whole table by repeating this operation box by box. It will be reiterated from the beginning of the table through the end minus one box each time until there is no more swap during an iteration. Thanks to this method, the detected points are classified by their horizontal position. Nevertheless, it must be remembered that the vertical location of the beam spots have to be taken into consideration since we want to order the points row by row from the left to the right. This means that the algorithm needs to be modified to arrange the x position of the points only in they belong to the same row. Thus, we swap the consecutive centroids if their horizontal position is not in an ascending order and also if they belong to the same row. As our grid is 10 x 10, we round to the lower ten the current box position (the numbering is from 0) to know at which row the spot is located.

These techniques are tested on the same grid as above, adding some noise (see figures 2.11(a) and 2.11(b)). To choose the adapted number of erosion and dilation to effectuate the opening, the size of the points have to be taken into account. Indeed, if too many erosions are carried out, all the beam spots will be removed. On the contrary, if not enough are accomplished, two linked spots will not be separated. Each point of the grid is composed of around 300 pixels. As we want to keep enough pixels to compute an accurate centroid, it is needed to keep at least 50 pixels. Four erosions allow to reach this result, followed by the same number of dilation to retrieve nearly the original number of pixels and to accomplish the opening. To make sure that the opening will only slightly change the centre of mass of the points, the centroiding method was performed on figure 2.10(a) with and without opening. The coordinates of the centroids were exactly the same in the two cases. The opening has preserved the information. It will

be assumed that even if there is a slight centroiding error after the opening, it is insignificant.

Several types of noise are added and are denoted figure 2.11(a).

- The first one shows that small changes of green color on a point or inside the same point do not affect the color detection, but could have an impact on the centroid as it is weighted by the intensity of the color.
- The second noise is a spot of a green-brown color. As it is expected, it is not detected by the color detection algorithm.
- The same spot (3 on the figure) but with a color close to the grid points is added to the image. It is detected as a point but its size is under the threshold chosen and it is dismissed as it can be seen on the figure 2.11(b). The opening also ensures that the unexpected spot disappears.
- The fourth noise represents two linked points. Thanks to the opening, which reduces the size of the beam spots before increasing them but not as much as they were originally, the connected points are well separated on the final image.
- In 5, a smaller green spot (which is noise) is linked to a real point. The spot is tiny and even if it is detected by the color algorithm, the opening is efficient enough to delete it as it is on the edge of a bigger beam spot.
- Finally, the last kind of noise tested (6) ... to be completed

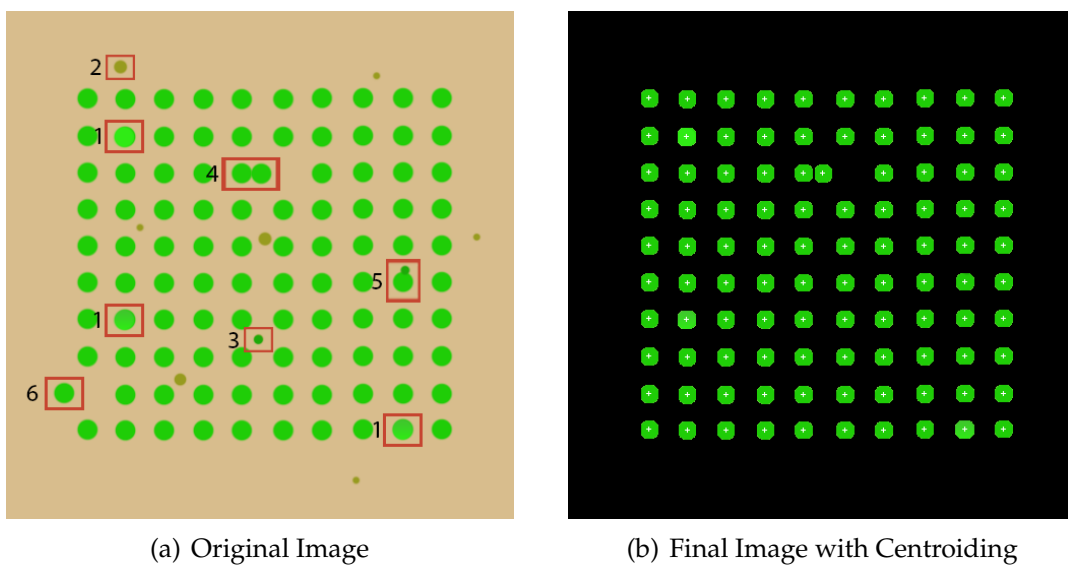


Figure 2.11: RGB images of a grid of 10 x 10 green points with noise

It can be concluded that the algorithm is robust enough to handle some noise on computed images. Nevertheless, the deformation and the unexpected light spots or reflets on the rocks could be worse than expected and the algorithm may be incapable of finding the centroid of each point, with no false positive or false negative. To ensure the robustness of the algorithm, integration tests with a real system have to be carried out.

Part 3

Experimental Results

3.1 Distances with Several Points

After the experiment with only one lighting dot, the next step is using several lighting points. Thus, the goal of this experiment is using several points in order to detect several distances in front of the camera.

3.1.1 Choices of Implementation

First of all, a grid of dots is supposed to be projected on the target. However, instead of a grid, a line of 10 dots is used during this experiment. Indeed, as the triangulation theory between a grid of and a line of dots is the same and the indexing of the dots of a grid is much more difficult than the one of the dots of a line, it has been chosen to use a line in order to focus on the improvement of the robustness and accuracy of the algorithm. Once these two goals completed, only the implementation of a function permitting the indexation of the dots of the grid would be needed to switch to a grid.

Then, as the purpose of this project is the vision analysis, the focus is on the structured light algorithm and the artificial light source has not been built. Thus, in order to be able to project a line of several dots on a target, it has been chosen to use an overhead projector. Indeed, even if a laser was available (see the first experiment), after trying to diffract its beam (using a CD for instance), it appeared that the brightness of each dot was very imbalanced (central dot very luminous compared to the others) and would lead to a modification of the parameters of the dot detection. Moreover, as the artificial light source is supposed to project a grid of identical dots, the overhead projector has been chosen to respect this equality of brightness.

3.1.2 Progress of the Experiment

A picture of a line of 10 green dots (a green close to the one of the laser) with a reddish background (in order to represent the color of the rocks of Mars) is projected on a board using the overhead projector. Then an object is placed between the board and the camera and the several distance z_i are computed (see Figure 3.1).

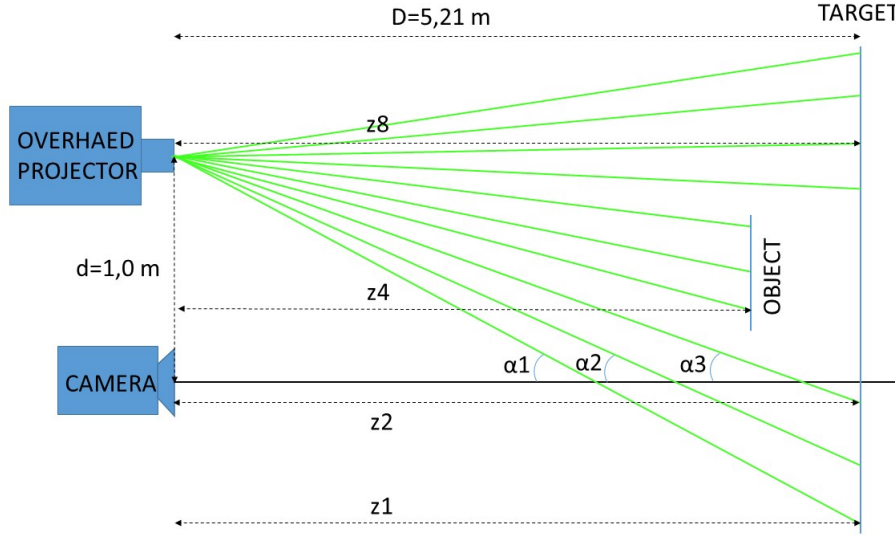


Figure 3.1: schema of the experiment

Once the script is run, the different steps are the following :

Step 1 : Calibration

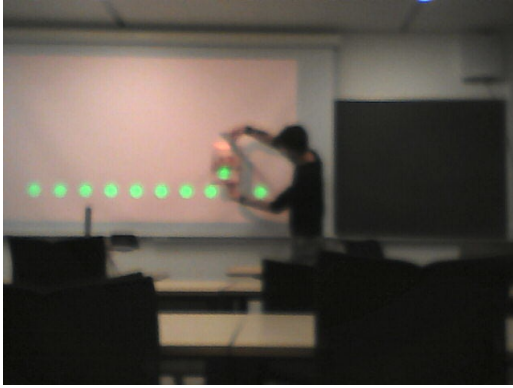
In order to find the different angles α_i between the focal axis of the camera and the beams of the projector, a calibration function is called before the real time loop. This function detects the lighting dots, their centroid and use the following formula to save the different $\tan \alpha_i$ into an array.

$$\tan \alpha_i = \frac{d}{D} - P_{pixels,i} \frac{P_{size}}{f_0}$$

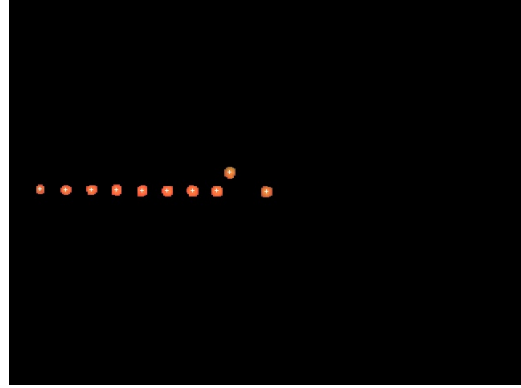
Step 2 : Positioning of the Object

During this step, while the script is still running, the object is placed between the camera and the board (see Figure 3.2(a)). On the one hand, as the projector is higher than the camera, it makes the 9th dot slide vertically. However, it does not affect the result as only the horizontal slide is taken into account and the *sort* function permits to keep the dots in the right order even if they slide vertically. On the other hand, a horizontal slide occurs as expected.

The experiment has been carried out with several distances and placing objects in front of several dots. Moreover, some noise has been added. As we can see figure 3.3(a), the background is nuanced, smaller dots with the same green are added and dots of the same size but with others greens are added too. We can see figure 3.3(b) that the algorithm manages to filter the different noises and still detects the 10 dots.

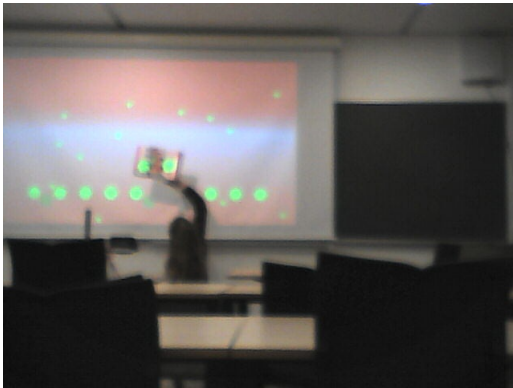


(a) Positioning of the object in front of the 9th dot

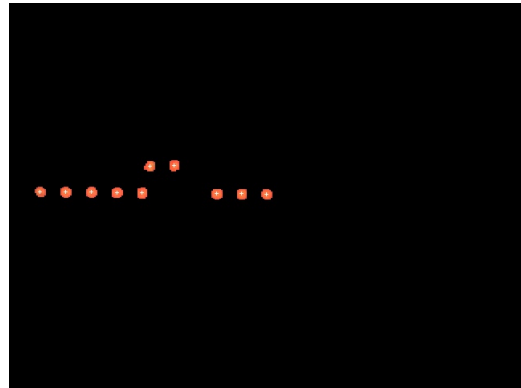


(b) Detection of the centroids

Figure 3.2: Distance object-board = 50 cm



(a) Positioning of the object in front of the 6th and 7th dots



(b) Detection of the centroids

Figure 3.3: Distance object-board = 90 cm

This experiment was carried out in real time, that is to say the several distances were displayed continuously. However, some pictures were saved in order to permit people to run the algorithm used during the experiment. Indeed, you can find into the folder '???????' the C++ script used and pictures of objects at several distances taken by the camera. Note that the script needs to be modified to use pictures instead of a video flux. Moreover, the Power Points used to project the dots and backgrounds are also present in order to permit the performing of

the experiment in real time but in this case, the distances camera-projector d and camera-target D need to be adapted and the calibration done.

3.1.3 Results

The results of the experiment for the different distances object-board are presented Tables 3.1, 3.2, 3.3 and 3.4.

Table 3.1: Object in front of dot 9 with distance object-board = 0.50 m (without noise)

i	z_i [m]	error ¹ [%]	distance board-Object [m]	error ¹ [%]
1	5.16205	0.92	0.048	
2	5.18899	0.40	0.021	
3	5.20282	0.14	0.007	
4	5.20879	0.02	0.001	
5	5.20999	0.00	0.000	
6	5.17524	0.67	0.035	
7	5.21324	0.06	-0.003	
8	5.22243	0.24	-0.012	
9	4.75529	0.01	0.455	9.06
10	5.27336	1.22	-0.063	

$$^1error = \frac{distance_{theory} - distance_{experiment}}{distance_{theory}} 100$$

Table 3.2: Object in front of dots 1 and 2 with distance object-board = 0.50 m (without noise)

i	z_i [m]	error [%]	distance board-Object [m]	error [%]
1	4.69081	0.41	0.519	3.84
2	4.74072	0.65	0.469	6.14
3	5.20312	0.13	0.007	
4	5.17385	0.69	0.036	
5	5.20999	0.00	0.000	
6	5.2103	0.01	-0.000	
7	5.21342	0.07	-0.003	
8	5.22243	0.24	-0.012	
9	5.24131	0.60	-0.031	
10	5.30847	1.89	-0.098	

Table 3.3: Object in front of dots 1 and 2 with distance object-board = 0.90 m (without noise)

i	z_i [m]	error [%]	distance board-Object [m]	error [%]
1	4.34553	0.82	0.864	3.95
2	4.36417	1.26	0.846	6.02
3	5.23825	0.54	-0.028	
4	5.2443	0.66	-0.034	
5	5.20999	0.00	0.000	
6	5.17524	0,67	0,035	
7	5.21324	0,06	-0,003	
8	5.22243	0,24	-0,012	
9	5.27727	1,29	-0,067	
10	5.23746	0,53	-0,027	

Table 3.4: Object in front of dots 6 and 7 with distance object-board = 0.70 m and noise

i	z_i [m]	error [%]	distance board-Object [m]	error [%]
1	5.16204	0.92	0.048	
2	5.18898	0.40	0.021	
3	5.20312	0.13	0.007	
4	5.20879	0.02	0.001	
5	5.20999	0.00	0.000	
6	4.53458	0.55	0.675	3.51
7	4.51034	0.01	0.700	0.04
8	5.22242	0.24	-0.012	
9	5.24131	0.60	-0.031	
10	5.30848	1.89	-0.09848	

3.1.4 Interpretations

As we can see on the Table 3.4, the errors of the results of the experiment with noise are in the same order of magnitude than the ones without noise. It means that the algorithm is robust enough to handle the noise. Indeed, the opening permitting the selection of only the dots of the projected pattern works well. Moreover, as we can see figure 3.2(a) and 3.3(a), the images recorded are very blurred because of the camera used (webcam Philips SPZ2000). As the results are acceptable, it means that the algorithm deals also with the blur, that is to say that it could even works if the target would get a bit out of the depth of field.

However, according to the four Tables, we can see that the errors of the distance object-board is between 0.04 and 9.06 %, which can be a significant error. Indeed, an error of 9.06 % represents an experimental distance of 455 mm instead of 500 which means an error of 45 mm. For instance, our target is supposed to be a rock at a distance between one and two meters. Let us assume that one of the projected dots is on a part of the rock which is 1500 mm far from the camera. An error of 9.06 % would lead to a measured distance of 1364 mm, that is to say an error of 136 mm. To have a negligible error, the rock should have a shape such as the depth would vary over a range of at least one meter. Therefore, it would definitely not be acceptable.

These errors come from the calibration and the detection of the centroids. Several aspects of the detection of the centroids could be improved. Indeed, the open-

ing used to ignore the noise modify the brightness of the dots, which may also change the position of the centroids. Moreover, as the brightness of the lighting dots is not uniform, that is to say it decreases with the distance from the center, the algorithm of color detection does not detect the same pixels over time, some bordering pixels are detected or not over time. This weakness of the color detection may also change the position of the centroids.

Nevertheless, we have to notice that during this experiment, the calibration was not rigorous. Indeed, the distances board-object, D and d were measured with a measure tape what is not precise enough. Also, the focal axis of the camera was not exactly perpendicular to the target as it is supposed to be according to the delimitation of the scene. Therefore, the errors of the measures of the distances should decrease with a precise calibration done with adapted tools. Moreover, as the overhead projector was fixed on the ceiling and the focal axis of the camera had to keep perpendicular to the target, we were not able to make the distance d vary. It could have been interesting to make the angles α vary in order to study the precision of the results according to these angles. Indeed, as it has been explained, the position of the centroids may vary a bit over time. Therefore, a bigger angle α would lead to a bigger distance p and thus variations of the centroids would have been more negligible.

3.1.5 Limits of the Experiment

The first limit of this experiment is that some pattern disorders are not taken into account. The permutation of dots that can happen with an object too far from the board has been prevented with a maximum distance board-object = 90 cm. With a greater distance than one meter, a permutation appears between the dots on the object and the ones at the left of the object but this permutation is not managed, corrected by the *sort* function. Another disorder not tested is the merger of two dots. As the projector was on the ceiling, projecting slightly downward, the dots shifted horizontally but also vertically and as a consequence, the dots on the object were too high to merge with the dots on the board. Even if this kind of disorder was tested during the integration tests 2.3.3, it would have been interesting to test it during the experiment. A second limit is that, as this experiment does not include several aspects of the system designed (projector instead of the artificial light source, line of dots instead of a grid, ...), it cannot be considered as a test of this last one. Nevertheless, it permits to test the accuracy and the robustness of the algorithm tested. It is only an integration test.

Appendix A

LED Properties

Caractéristiques

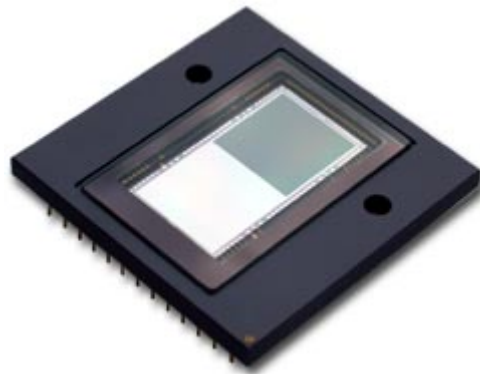
• Couleur	Vert
• Température de couleur	525nm
• Intensité Lumineuse	84000mcd
• Ampérage Requis	20mA
• Angle de Diffusion	30°
• Consommation	220mW
• Tension d'alimentation	9.3 - 10.5V
• Durée de vie estimée	80 000 Heures

Figure A.1: LED Datasheet

Appendix B

CCD Properties

DATA SHEET



FTT1010M

1M Frame Transfer CCD Image Sensor

Product specification

2007, April 17

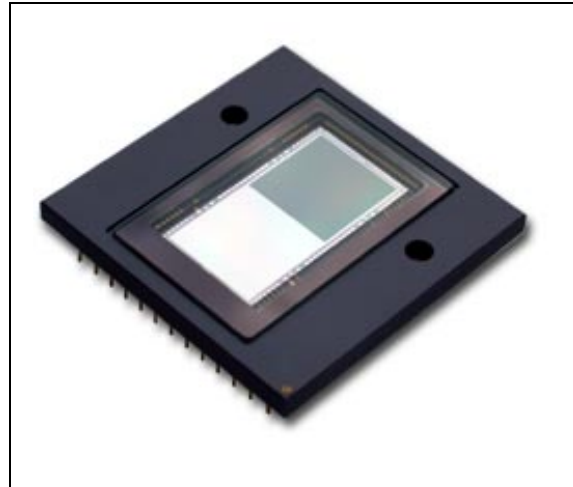
DALSA
Professional Imaging



1M Frame Transfer CCD Image Sensor

FTT1010M

- 1-inch optical format
- 1M active pixels (1024H x 1024V)
- Progressive scan
- Excellent antiblooming
- Variable electronic shuttering
- Square pixel structure
- H and V binning
- 100% fill factor
- High dynamic range (>72dB)
- High sensitivity
- Low dark current and fixed pattern noise
- Low readout noise
- Data rate up to 2 x 40 MHz
- Mirrored and split readout
- RoHS compliant



Description

The FTT1010M is a monochrome progressive-scan frame-transfer image sensor offering 1K x 1K pixels at 30 frames per second through a single output buffer. The combination of high speed and a high linear dynamic range (>12 true bits at room temperature without cooling) makes this device the perfect solution for high-end real time medical X-ray, scientific and industrial applications. A second output can either be used for mirrored images, or can be read out simultaneously with other output to double the frame rate. The device structure is shown in figure 1.

Device structure

Optical size:	12.288 mm (H) x 12.288 mm (V)
Chip size:	14.572 mm (H) x 26.508 mm (V)
Pixel size:	12 μ m x 12 μ m
Active pixels:	1024 (H) x 1024 (V)
Total no. of pixels:	1072 (H) x 1030 (V)
Optical black pixels:	Left: 20 Right: 20
Timing pixels:	Left: 4 Right: 4
Dummy register pixels:	Left: 7 Right: 7
Optical black lines:	Bottom: 6 Top: 6

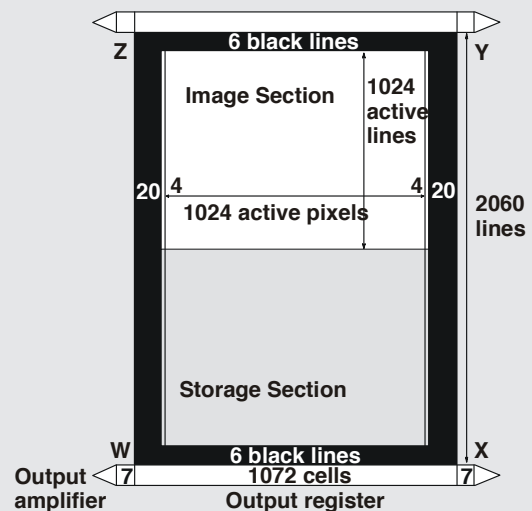


Figure 1 – Device Structure

1M Frame Transfer CCD Image Sensor

FTT1010M

Architecture of the FTT1010M

The FTT1010M consists of a shielded storage section and an open image section. Both sections are electronically the same and have the same cell structure with the same properties. The only difference between two sections is the optical light shield.

The optical centres of all pixels in the image section form a square grid. The charge is generated and integrated in this section. Output registers are located below the storage section. The output amplifiers Y and Z are not used in Frame Transfer mode and should be connected as not-used amplifiers.

After the integration time, the charge collected in the image section is shifted to the storage section. The charge is read out line by line through the lower output register.

The left and the right half of each output register can be controlled independently. This enables either single or multiple readout.

During vertical transport, the C3 gates separate the pixels in the register. The letters W, X, Y, and Z are used to define the four quadrants of the sensor. The central C3 gates of both registers are part of the W and Z quadrants of the sensor.

Both upper and lower registers can be used for vertical binning. Both registers also have a summing gate at each end that can be used for horizontal binning. Figure 2 shows the detailed internal structure.

IMAGE SECTION	
Image diagonal (active video only)	17.38 mm
Aspect ratio	1:1
Active image width x height	12.288 x 12.288 mm ²
Pixel width x height	12 x 12 μm^2
Fill factor	100%
Image clock pins	A1, A2, A3, A4
Capacity of each clock phase	2.5nF per pin
Number of active lines	1024
Number of black reference lines	6
Total number of lines	1030
Number of active pixels per line	1024
Number of overscan (timing) pixels per line	8 (2x4)
Number of black reference pixels per line	40 (2x20)
Total number of pixels per line	1072
STORAGE SECTION	
Storage width x height	12.864 x 12.360 mm ²
Cell width x height	12 x 12 μm^2
Storage clock phases	B1, B2, B3, B4
Capacity of each clock phase	2.5nF per pin
Number of cells per line	1072
Number of lines	1030
OUTPUT REGISTERS	
Output buffers (three-stage source follower)	4 (one on each corner)
Number of registers	2 (one above, one below)
Number of dummy cells per register	14 (2x7)
Number of register cells per register	1072
Output register horizontal transport clock pins	C1, C2, C3
Capacity of each C-clock phase	60pF per pin
Overlap capacity between neighbouring C-clocks	20pF
Output register Summing Gates	4 pins (SG)
Capacity of each SG	15pF
Reset Gate clock phases	4 pins (RG)
Capacity of each RG	15pF

1M Frame Transfer CCD Image Sensor

FTT1010M

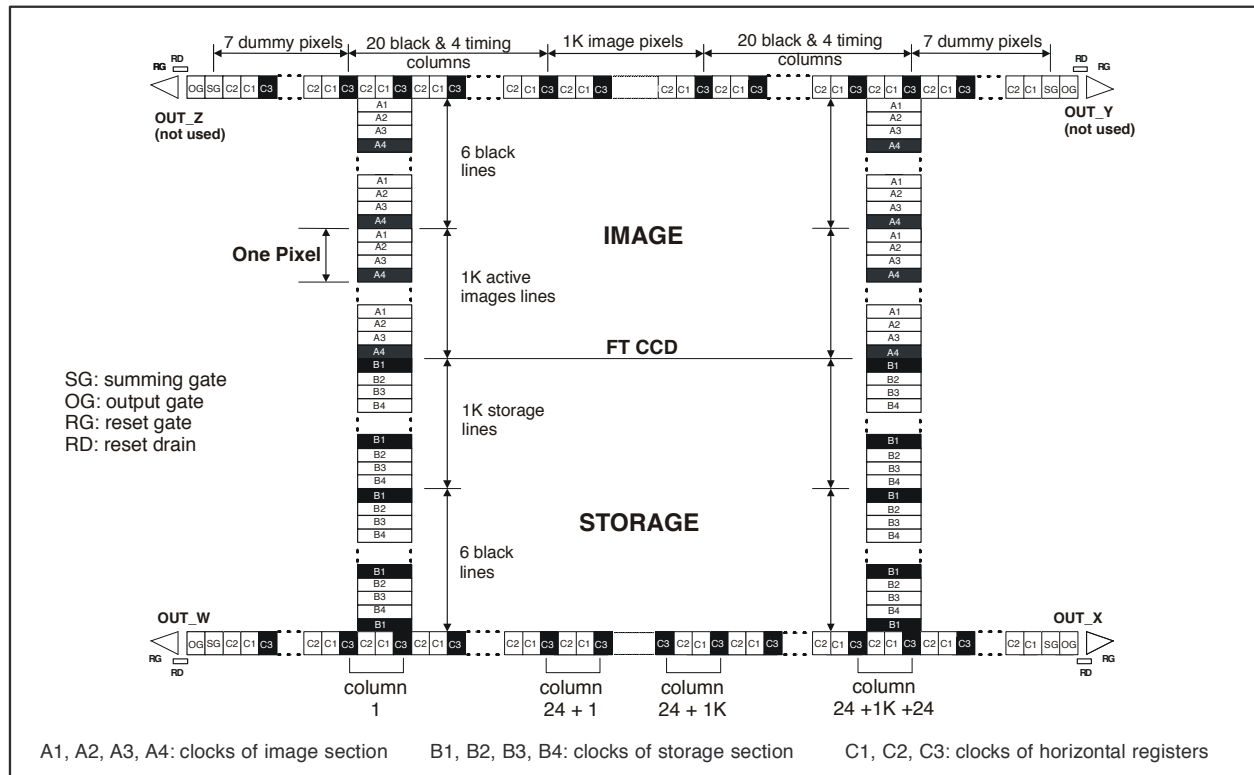


Figure 2 - Detailed internal structure

1M Frame Transfer CCD Image Sensor

FTT1010M

Specifications

ABSOLUTE MAXIMUM RATINGS ¹		MIN	MAX	UNIT	
GENERAL:					
storage temperature		-55	+80		°C
ambient temperature during operation		-40	+60		°C
voltage between any two gates		-20	+20		V
DC current through any clock (absolute value)		-0.2	+0.2		μA
OUT current (no short circuit protection)		0	10		mA
VOLTAGES IN RELATION TO VPS:					
VPS, SFD, RD		-0.5	+30		V
VCS, SFS		-8	+5		V
All other pins		-5	+25		V
VOLTAGES IN RELATION TO VNS:					
SFD, RD		-15	+0.5		V
VCS, SFS, VPS		-30	+0.5		V
All other pins		-30	+0.5		V
DC CONDITIONS ^{2,3}		MIN [V]	TYPICAL [V]	MAX [V]	MAX [mA]
VNS ⁴	N substrate	20	24	28	15
VPS	P substrate	1	3	7	15
SFD	Source Follower Drain	16	20	24	4.5
SFS	Source Follower Source	-	0	-	1
VCS	Current Source	-5	0	3	-
OG	Output Gate	4	6	8	-
RD	Reset Drain	13	15.5	18	-
AC CLOCK LEVEL CONDITIONS ²		MIN	TYPICAL	MAX	UNIT
IMAGE CLOCKS:					
A-clock amplitude during integration and hold		8	10		V
A-clock amplitude during vertical transport (duty cycle=5/8) ⁵		10	14		V
A-clock low level			0		V
Charge Reset (CR) level on A-clock ⁶		-5	-5		V
STORAGE CLOCKS:					
B-clock amplitude during hold		8	10		V
B-clock amplitude during vertical transport (duty cycle=5/8)		10	14		V
OUTPUT REGISTER CLOCKS:					
C-clock amplitude (duty cycle during hor. transport=3/6)		4.75	5	5.25	V
C-clock low level		2	3.5		V
Summing Gate (SG) amplitude			10	10	V
Summing Gate (SG) low level			3.5		V
OTHER CLOCKS:					
Reset Gate (RG) amplitude		5	10	10	V
Reset Gate (RG) low level			3		V
Charge Reset (CR) pulse on Nsub ⁶		0	10	10	V

¹ During Charge Reset it is allowed to exceed maximum rating levels (see note 5)² All voltages in relation to SFS³ Power-up sequence: VNS, SFD, RD, VPS, others⁴ To set the VNS voltage for optimal Vertical Antiblooming (VAB), it should be adjustable between minimum and maximum values⁵ Three-level clock is preferred for maximum charge; the swing during vertical transport should be 4V higher than the voltage during integration
A two level clock (typically 10V) can be used if a lower maximum charge handling capacity is allowed⁶ Charge Reset can be achieved in two ways:

- The typical CR level is applied to all image clocks simultaneously (preferred).
- The typical A-clock low level is applied to all image clocks; for proper CR, an additional Charge Reset pulse on VNS is required. This will also affect the charge handling capacity in the storage areas.

1M Frame Transfer CCD Image Sensor

FTT1010M

Timing diagrams (for default operation)

AC CHARACTERISTICS	MIN	TYPICAL	MAX	UNIT
Horizontal frequency ($1/Tp$) ¹	0	18	40	MHz
Vertical frequency	0	450	1000	kHz
Charge Reset (CR) time	2	20		μs
Rise and fall times: image clocks (A)	10	20		ns
storage clocks (B)	10	20		ns
register clocks (C) ²	3	5	1/6 Tp	ns
summing gate (SG)	3	5	1/6 Tp	ns
reset gate (RG)	3	5	1/6 Tp	ns

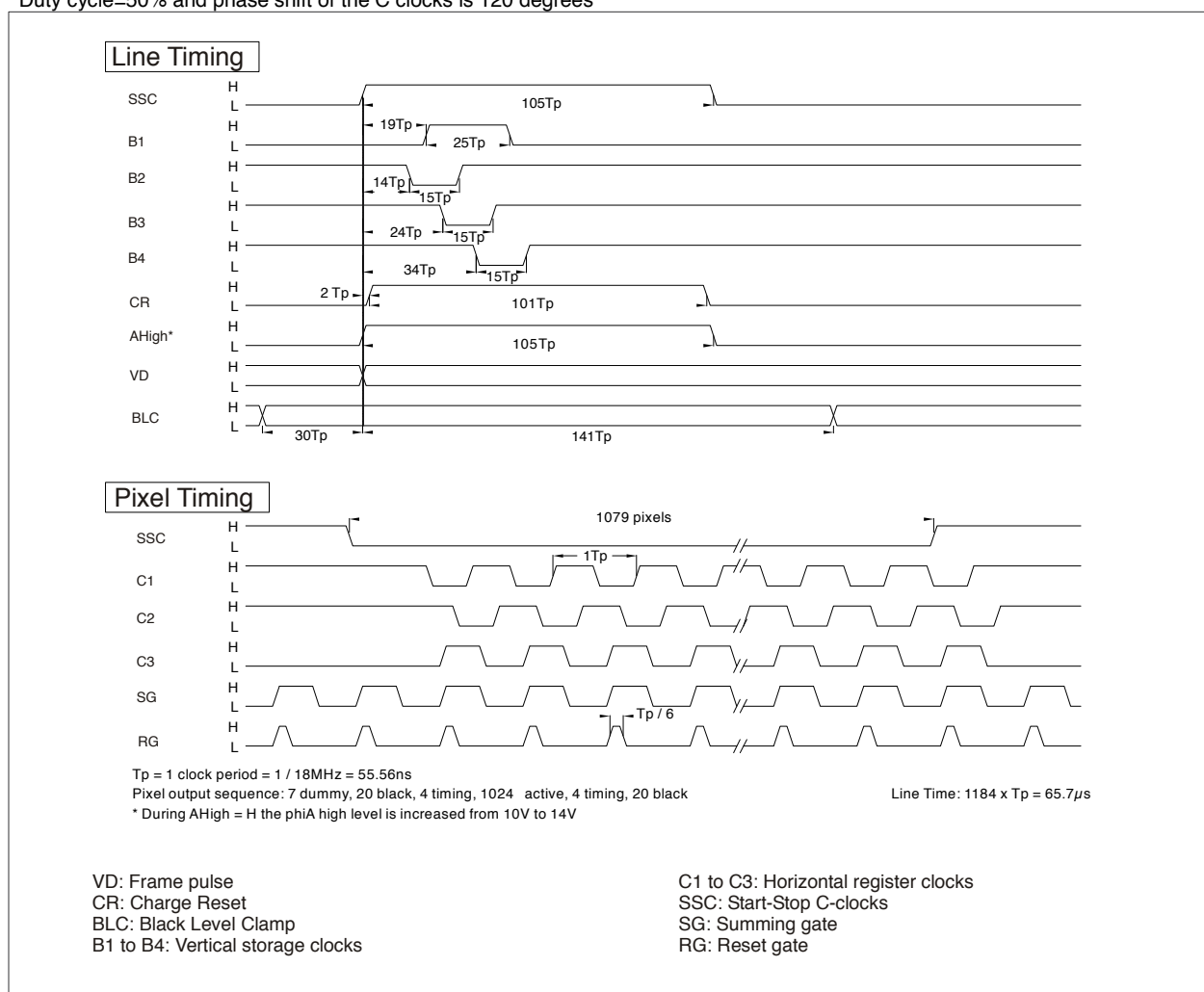
¹ TP=1 clock period² Duty cycle=50% and phase shift of the C clocks is 120 degrees

Figure 3 - Line and pixel timing diagrams

1M Frame Transfer CCD Image Sensor

FTT1010M

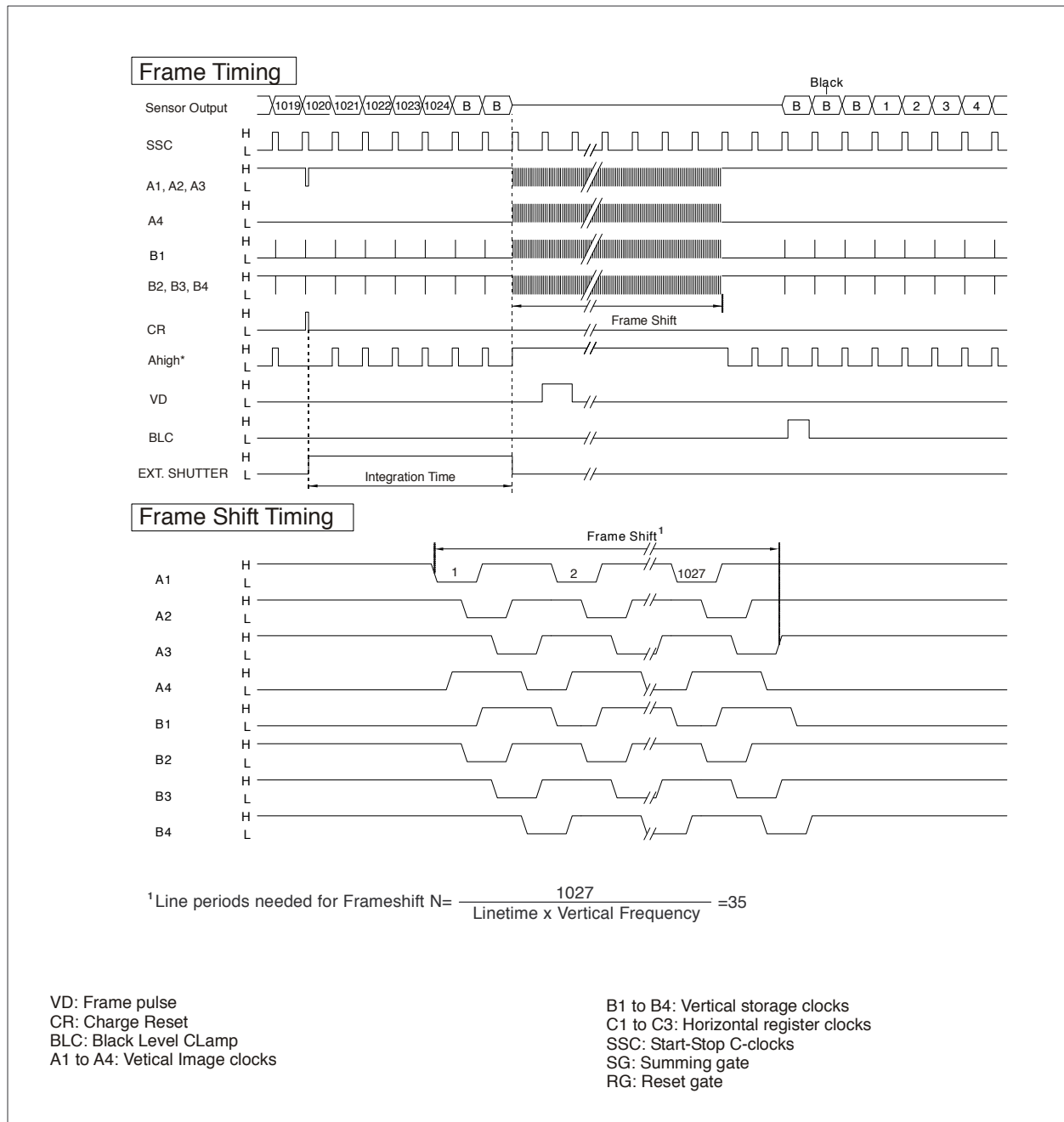


Figure 4 - Frame timing diagrams

1M Frame Transfer CCD Image Sensor

FTT1010M

Line timing

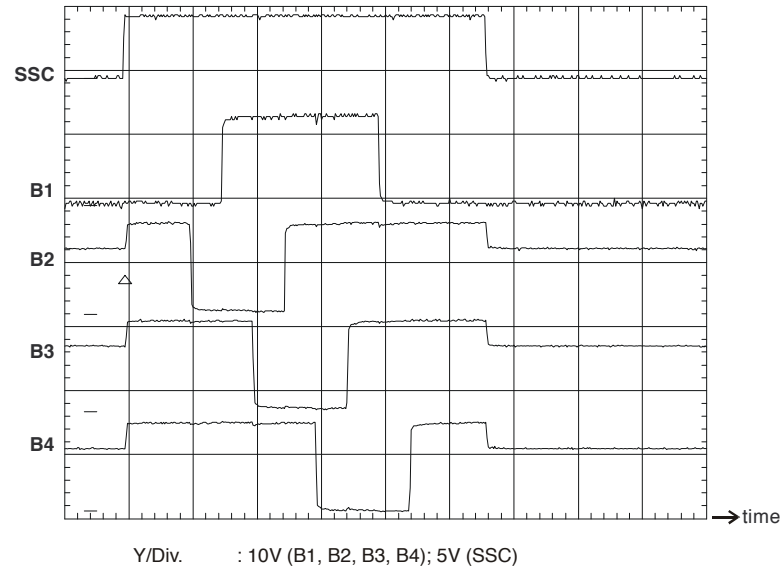


Figure 5 - Vertical readout

Pixel timing

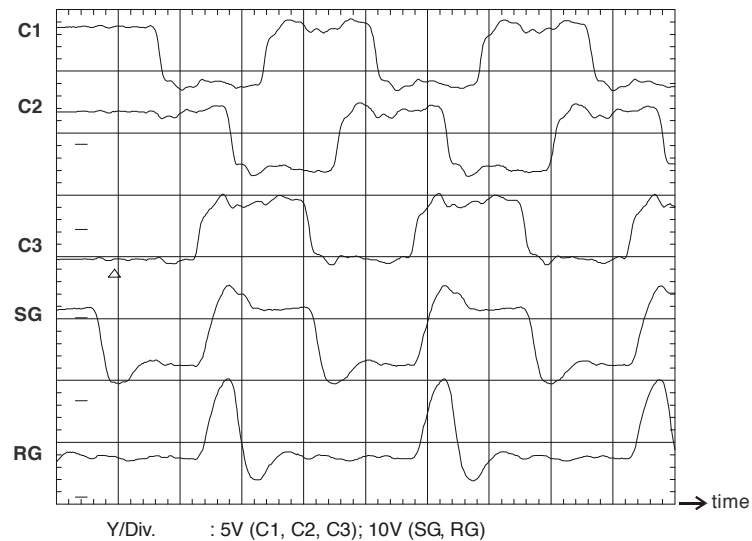


Figure 6 - Start horizontal readout

1M Frame Transfer CCD Image Sensor

FTT1010M

Performance

The test conditions for the performance characteristics are as follows:

- All values are measured using typical operating conditions.
- VNS is adjusted as low as possible while maintaining proper Vertical Antiblooming
- Sensor temperature=60°C (333K)
- Horizontal transport frequency=18MHz
- Vertical transport frequency=450kHz
- Integration time=10ms
- The light source is a lamp of 3200K in conjunction with neutral density filters and a 1.7mm thick BG40 infrared cut-off filter. For Linear Operation measurements, a temperature conversion filter (Melles Griot type no. 03FCG261, -120 mired, thickness: 2.5mm) is applied.

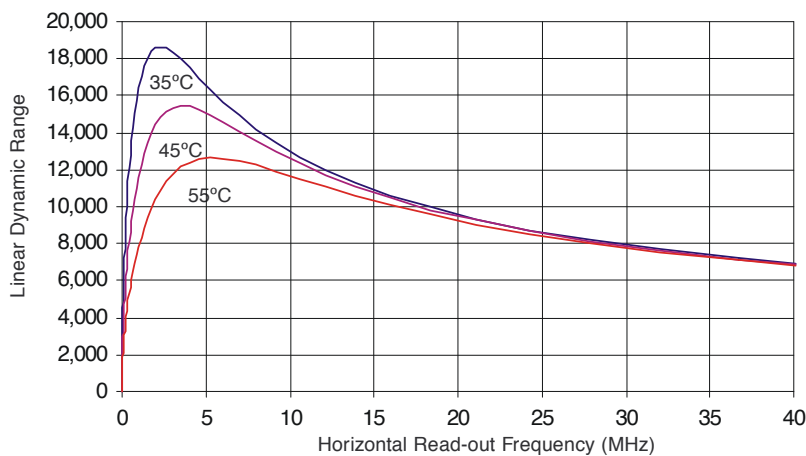
LINEAR OPERATION	MIN	TYPICAL	MAX	UNIT
Charge Transfer Efficiency ¹ vertical		0.999995		
Charge Transfer Efficiency ¹ horizontal		0.999999		
Image lag			0	%
Smear ²		-39	0	dB
Resolution (MTF) @ 42lp/mm	65			%
Light sensitivity	180	250		kel/lux*s
Low Pass Shading ³			2.5	%
Random Non-Uniformity (RNU) ⁴		0.3	5	%

¹Charge Transfer Efficiency values are tested by evaluation and expressed as the value per gate transfer.

²Smear is defined as the ratio of 10% of the vertical transport time to the integration time. It indicates how visible a spot of 10% of the image height would become.

³Low Pass Shading is defined as the ratio of the one- σ value of the pixel output distribution expressed as a percentage of the mean value output (low-pass image).

⁴RNU is defined as the ratio of the one- σ value of the highpass image to the mean signal value at nominal light.



Linear dynamic range is defined as the ratio of Q_{lin} to read-out noise (the latter reduced by Correlated Double Sampling).

Figure 7 - Typical Linear dynamic range vs. horizontal read-out frequency and sensor temperature

1M Frame Transfer CCD Image Sensor

FTT1010M

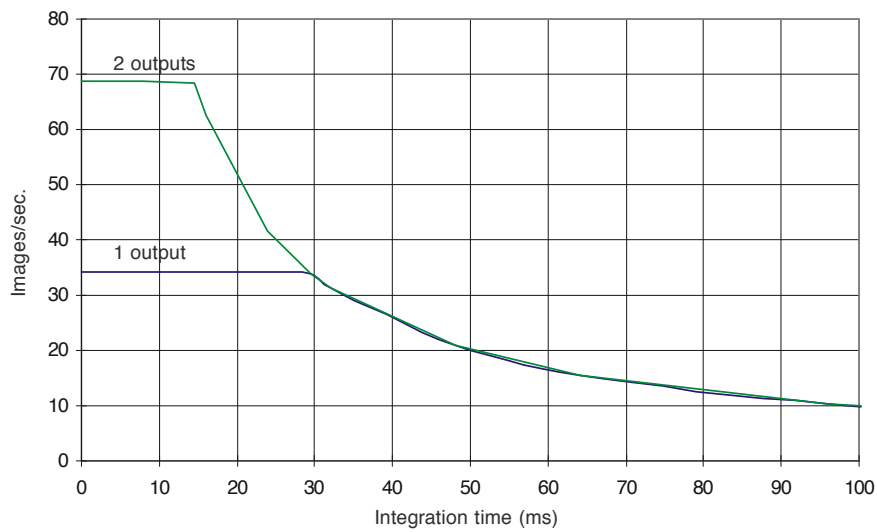


Figure 8 - Maximum number of images/second versus integration time

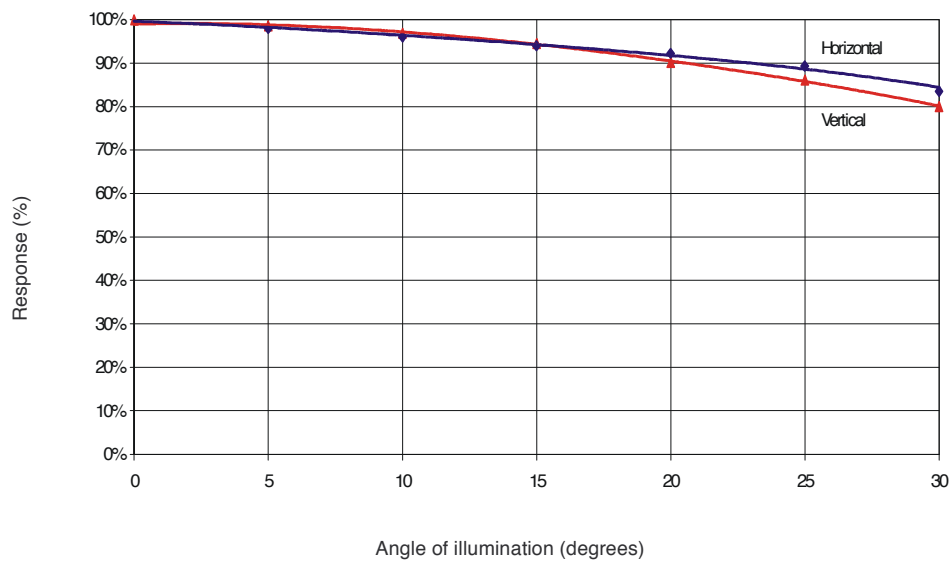


Figure 9 - Angular response versus angle of illumination

1M Frame Transfer CCD Image Sensor

FTT1010M

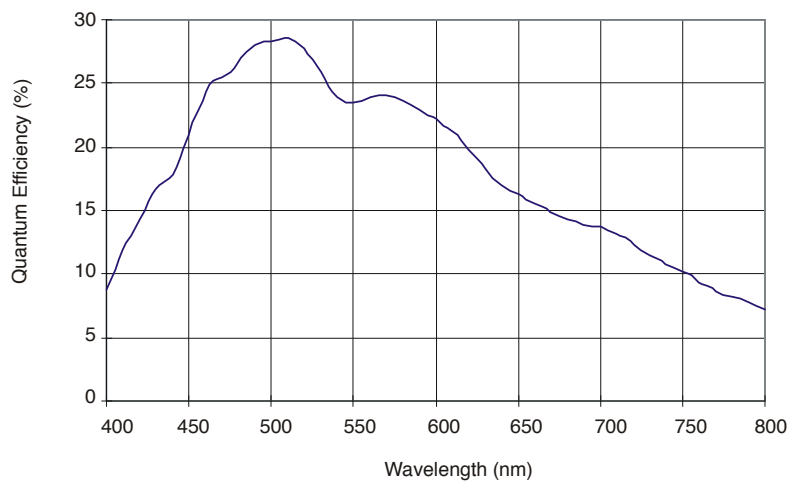


Figure 10 - Quantum efficiency versus wavelength

1M Frame Transfer CCD Image Sensor

FTT1010M

LINEAR/SATURATION	MIN	TYPICAL	MAX	UNIT
Full-well capacity saturation level (Qmax) ¹	250	500	600	kel
Full-well capacity linear operation (Qlin) ²	200	350		kel
Charge handling capacity ³		600		kel
Overexposure ⁴ handling	100	200		x Qmax level

¹Qmax is determined from the low-pass filtered image.

²The linear full-well capacity Qlin is calculated from linearity test (see dynamic range). The evaluation test guarantees 97% linearity.

³Charge handling capacity is the largest charge packet that can be transported through the register and read-out through the output buffer.

⁴Overexposure over entire area while maintaining good Vertical Antiblooming (VAB). It is tested by measuring the dark line.

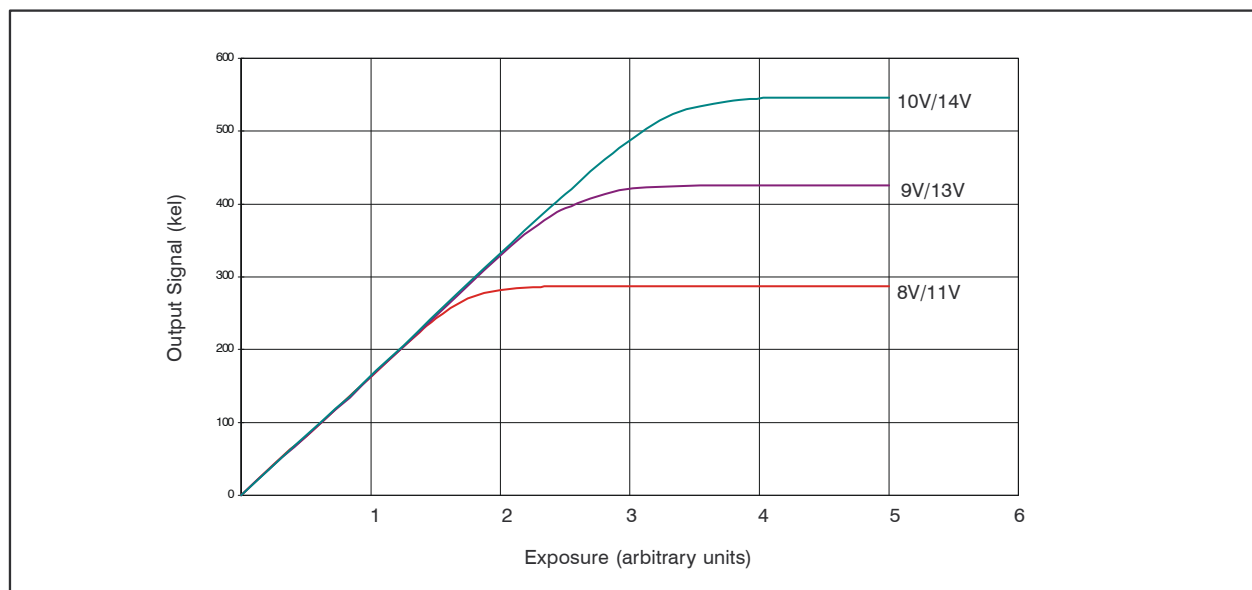


Figure 11 – Charge handling versus integration/transport voltage

1M Frame Transfer CCD Image Sensor

FTT1010M

OUTPUT BUFFERS	MIN	TYPICAL	MAX	UNIT
Conversion factor	6	8	12	$\mu\text{V}/\text{el}$
Mutual conversion factor matching (ΔACF) ¹		0	2	$\mu\text{V}/\text{el}$
Supply current		4		mA
Bandwidth		110		MHz
Output impedance buffer ($R_{\text{load}}=3.3\Omega$, $C_{\text{load}}=2\text{pF}$)		400		Ω

¹Matching of the four outputs is specified as ΔACF with respect to reference measured at the operating point ($Q_{\text{lin}}/2$)

DARK CONDITION	MIN	TYPICAL	MAX	UNIT
Dark current level @ 20°C		10	30	pA/cm^2
Dark current level @ 60°C		0.3	0.6	nA/cm^2
Fixed Pattern Noise ¹ (FPN) @ 60°C		15	25	el
RMS readout noise @ 9MHz bandwidth after CDS		25	30	el

¹FPN is one- σ value of the high-pass image.

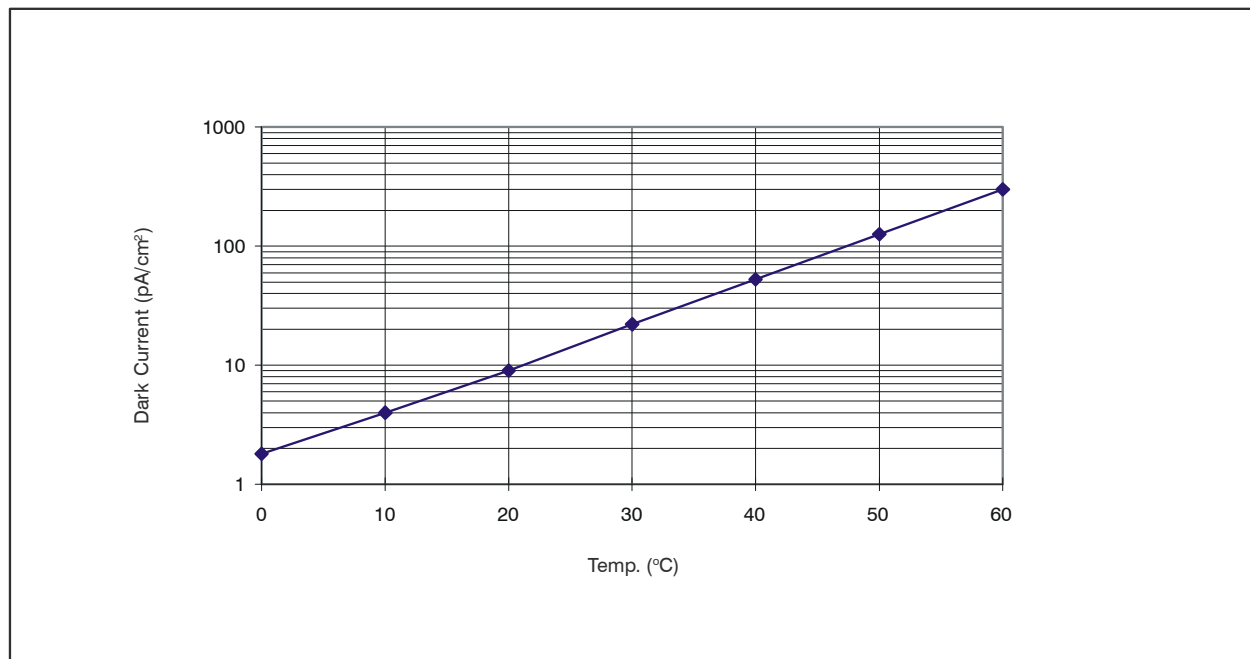


Figure 12 – Dark current versus temperature

1M Frame Transfer CCD Image Sensor

FTT1010M

Application information

Current handling

One of the purposes of VPS is to drain the holes that are generated during exposure of the sensor to light. Free electrons are either transported to the VRD connection and, if excessive (from overexposure), free electrons are drained to VNS. No current should flow into any VPS connection of the sensor. During high overexposure a total current of 10 to 15mA through all VPS connections together may be expected. The PNP emitter follower in the circuit diagram (figure 12) serves these current requirements.

VNS drains superfluous electrons as a result of overexposure. In other words, it only sinks current. During high overexposure, a total current of 10 to 15mA through all VNS connections together may be expected. The clamp circuit, consisting of the diode and electrolytic capacitor, enables the addition of a Charge Reset (CR) pulse on top of an otherwise stable VNS voltage. To protect the CCD, the current resulting from this pulse should be limited. This can be accomplished by designing a pulse generator with a rather high output impedance.

Decoupling of DC voltages

All DC voltages (not VNS, which has additional CR pulses as described above) should be decoupled with a 100nF decoupling capacitor. This capacitor must be mounted as close as possible to the sensor pin. Further noise reduction (by bandwidth limiting) is achieved by the resistors in the connections between the sensor and its voltage supplies. The electrons that build up the charge packets that will reach the floating diffusions only add up to a small current, which will float through VRD. Therefore, a large series resistor in the VRD connection may be used.

Outputs

To limit the on-chip power dissipation, the output buffers are designed with open source outputs. Outputs to be used should therefore be loaded with a current source or more simply with a resistance to GND. In order to prevent the output (which typically has an output impedance of about 400Ω) from bandwidth limitation as a result of capacitive loading, load the output with an emitter follower built from a high-frequency transistor. Mount the base of this transistor as close as possible to the sensor and keep the connection between the emitter and the next stage short. The CCD output buffer can easily be destroyed by ESD. By using this

emitter follower, this danger is suppressed; do NOT reintroduce this danger by measuring directly on the output pin of the sensor with an oscilloscope probe. Instead, measure on the output of the emitter follower. Slew rate limitation is avoided by avoiding a too-small quiescent current in the emitter follower; about 10mA should do the job. The collector of the emitter follower should be decoupled properly to suppress the Miller effect from the base-collector capacitance.

A CCD output load resistor of 3.3Ω typically results in a bandwidth of 110MHz. The bandwidth can be enlarged to about 130MHz by using a resistor of 2.2kΩ instead, which, however, also enlarges the on-chip power dissipation.

Device protection

The output buffers of the FTT1010M are likely to be damaged if VPS rises above SFD or RD at any time. This danger is most realistic during power-on or power-off of the camera. The RD voltage should always be lower than the SFD voltage.

Never exceed the maximum output current. This may damage the device permanently. The maximum output current should be limited to 10mA. Be especially aware that the output buffers of these image sensors are very sensitive to ESD damage.

Because of the fact that our CCDs are built on an n-type substrate, we are dealing with some parasitic npn transistors. To avoid activation of these transistors during switch-on and switch-off of the camera, we recommend the application diagram of figure 12.

Unused sections

To reduce power consumption, the following steps can be taken. Connect unused output register pins (C1...C3, SG, OG) and unused SFS pins to zero Volts.

More information

Detailed application information is provided in the application note AN01 entitled "**Camera Electronics for the mK x nK CCD Image Sensor Family**".

1M Frame Transfer CCD Image Sensor

FTT1010M

Device Handling

An image sensor is a MOS device which can be destroyed by electro-static discharge (ESD). Therefore, the device should be handled with care.

Always store the device with short-circuiting clamps or on conductive foam. Always switch off all electric signals when inserting or removing the sensor into or from a camera (the ESD protection in the CCD image sensor process is less effective than the ESD protection of standard CMOS circuits).

Being a high quality optical device, it is important that the cover glass remain undamaged. When handling the sensor, use **fingercots**.

When cleaning the glass we recommend using ethanol (or possibly water). Use of other liquids is strongly discouraged:

- if the cleaning liquid evaporates too quickly, rubbing is likely to cause ESD damage.
- the cover glass and its coating can be damaged by other liquids.

Rub the window carefully and slowly.

Dry rubbing of the window may cause electro-static charges or scratches which can destroy the device.

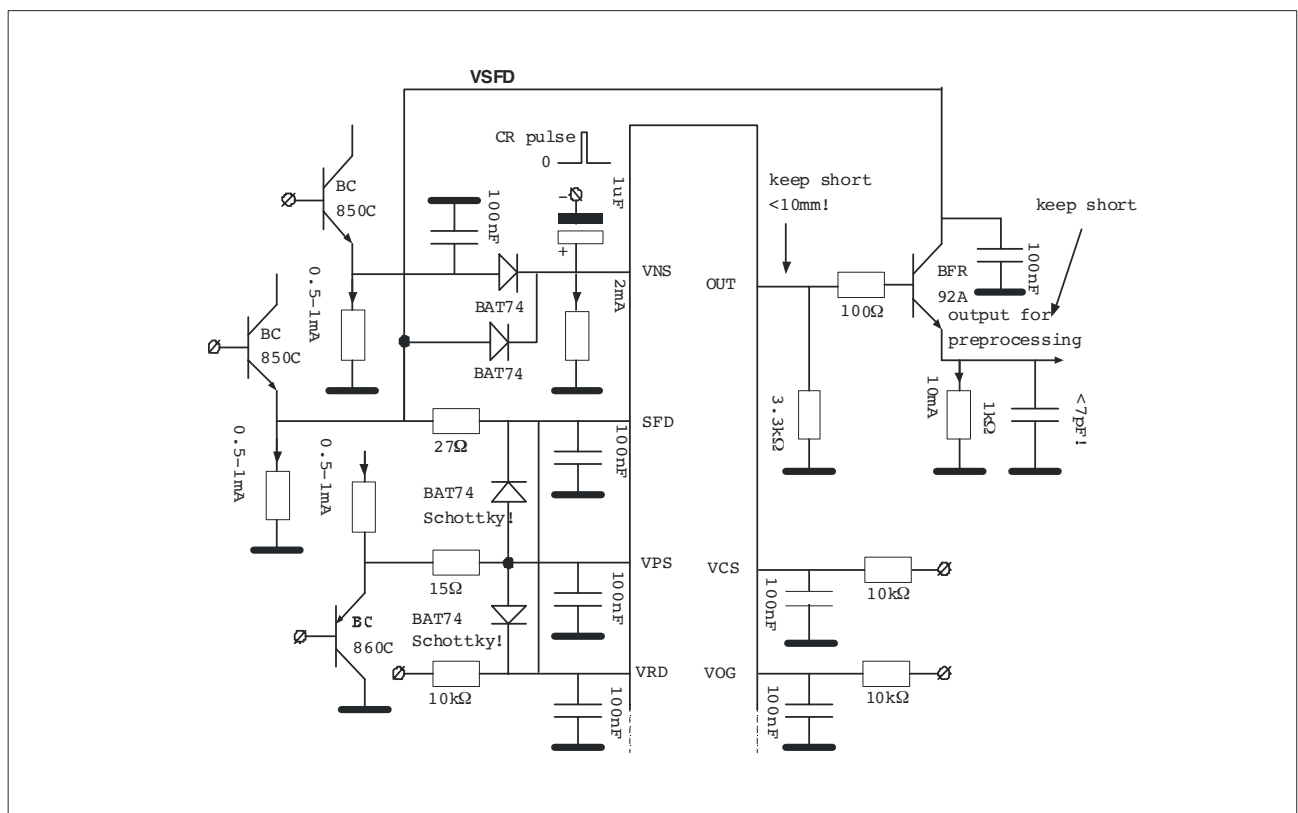


Figure 13– Application diagram

1M Frame Transfer CCD Image Sensor

FTT1010M

Pin configuration

The FTT1010M is mounted in a Pin Grid Array (PGA) package with 80 pins in a 15x13 grid of 40.00 x 40.00 mm². The position of pin A1 is marked with a gold dot on top of the

package. The image clock phases of quadrant W are internally connected to X, and the clock phases of Y are connected to Z.

SYMBOL	LINEAR/SATURATION	PIN # W	PIN # X	PIN # Y	PIN # Z
VNS	N substrate	A12	A3	J2	F11
VNS	N substrate	D11	B2	F3	H12
VNS	N substrate	E11	D3	-	J11
VNS	N substrate	E12	E2	-	-
VNS	N substrate	-	E3	-	-
VPS	P substrate	C11	C3	G3	G11
SFD	Source Follower Drain	A13	A1	J1	J13
SFS	Source Follower Source	A10	B5	J4	H9
VCS	Current Source	A11	A4	J3	J10
OG	Output Gate	B13	B1	H1	H13
RD	Reset Drain	B12	B3	H2	H11
A1	Image Clock (Phase 1)	-	-	F1	F13
A2	Image Clock (Phase 2)	-	-	G2	G12
A3	Image Clock (Phase 3)	-	-	F2	F12
A4	Image Clock (Phase 4)	-	-	G1	G13
B1	Storage Clock (Phase 1)	D13	D1	-	-
B2	Storage Clock (Phase 2)	C12	C2	-	-
B3	Storage Clock (Phase 3)	D12	D2	-	-
B4	Storage Clock (Phase 4)	C13	C1	-	-
C1	Register Clock (Phase 1)	B9	A6	H5	J8
C2	Register Clock (Phase 2)	B8	A7	H6	J7
C3	Register Clock (Phase 3)	A8	B6	J6	H8
SG	Summing Gate	B10	A2	H4	J12
RG	Reset Gate	A9	A5	J5	J9
OUT	Output	B11	B4	H3	H10
NC	Not Connected	B7		H7	

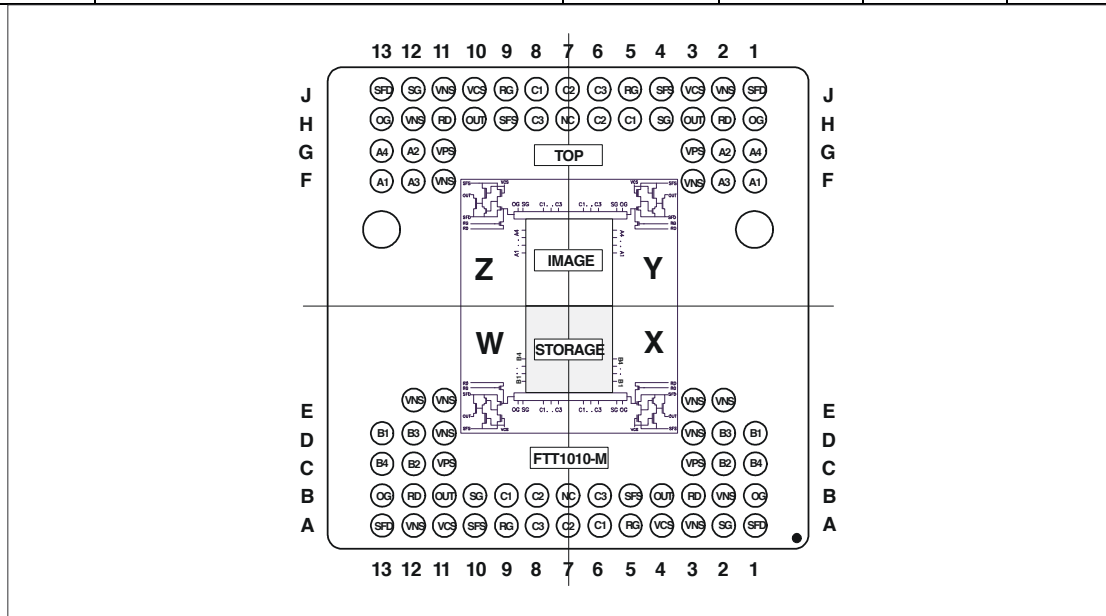


Figure 14 - Pin configuration (top view)

1M Frame Transfer CCD Image Sensor

FTT1010M

Package information

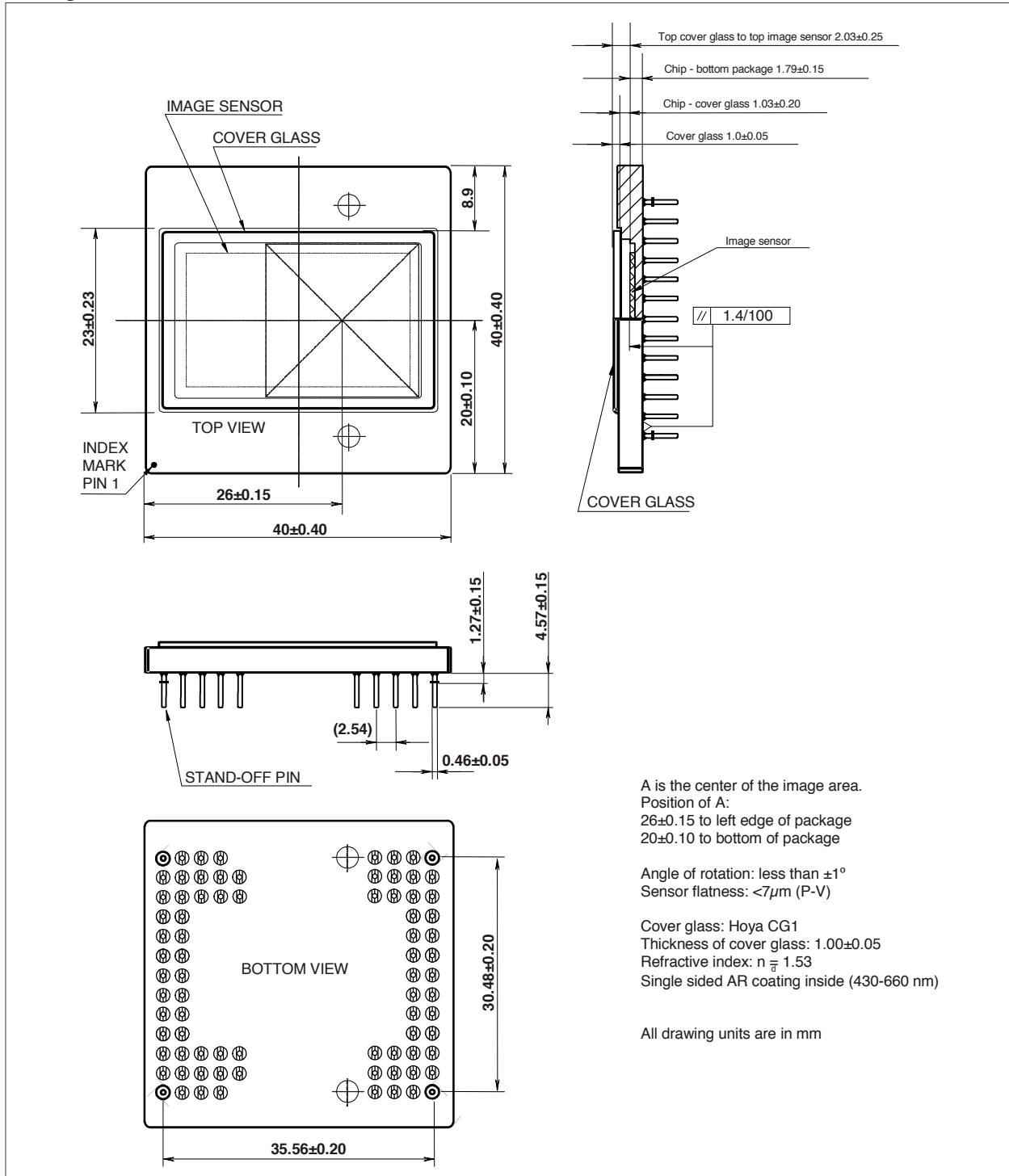


Figure 15– Mechanical drawing of the PGA package of the FTT1010M

1M Frame Transfer CCD Image Sensor

FTT1010M

Order codes

The sensor can be ordered using the following code:

FTT1010M sensors		
Description	Quality Grade	Order Code
FTT1010M/TG	Test grade	9922 157 35231
FTT1010M/EG	Economy grade	9922 157 35251
FTT1010M/IG	Industrial grade	9922 157 35221
FTT1010M/HG	High grade	9922 157 35211

**Defect Specifications**

The CCD image sensor can be ordered in a specific quality grade. The grading is defined with the maximum amount of pixel defects, column defects, row defects and cluster defects, in both illuminated and non-illuminated conditions. For detailed grading information, please contact your local DALSA representative.

For More Information

For more detailed information on this and other products, contact your local rep or visit our Web site at <http://www.dalsa.com/sensors/products/products.asp>.

DALSA Professional Imaging

Sales Department
High Tech Campus 27
5656 AE Eindhoven
The Netherlands
Tel: +31 40 259 9009
Fax: +31 40 259 9015
www.dalsa.com/sensors
sales.sensors@dalsa.com

This information is subject to change without notice.



Bibliography

- [1] Hubblesite. <http://hubblesite.org/newscenter/archive/releases/2001/31/image/a/>. Accessed: December 11, 2015.
- [2] Nasa mars orbiter catches twister in action. <http://mars.nasa.gov/mro/news/whatsnew/index.cfm?FuseAction=ShowNews&NewsID=1210>. Accessed: December 11, 2015.
- [3] Gary Bradski and Adrian Kaehler. *Learning OpenCV: Computer vision with the OpenCV library*. " O'Reilly Media, Inc.", 2008.
- [4] Jason Geng. Structured-light 3d surface imaging: a tutorial. *Advances in Optics and Photonics*, 3(2):128–160, 2011.
- [5] Berthold Horn. *Robot vision*. MIT press, 1986.
- [6] John Leif Jørgensen, 2015.
- [7] Hubert H Lamb. Climate present past and future vol-1. 1975.
- [8] JN Maki, JF Bell, KE Herkenhoff, SW Squyres, A Kiely, M Klimesh, M Schwochert, T Litwin, R Willson, A Johnson, et al. Mars exploration rover engineering cameras. *Journal of Geophysical Research: Planets* (1991–2012), 108(E12), 2003.
- [9] Hiroyoshi Morita, Kaanyasn Yajima, and Shojiro Sakata. Reconstruction of surfaces of 3-d objects by m-array pattern projection method. In *Computer Vision., Second International Conference on*, pages 468–473. IEEE, 1988.
- [10] NASA. Robotic mars exploration, 2015. [Online; accessed December 11, 2015].
- [11] Giovanna Sansoni, Marco Trebeschi, and Franco Docchio. State-of-the-art and applications of 3d imaging sensors in industry, cultural heritage, medicine, and criminal investigation. *Sensors*, 9(1):568–601, 2009.

- [12] Wikipedia. Atmosphère de mars — Wikipedia, the free encyclopedia, 2015. [Online; accessed December 11, 2015].
- [13] Wikipedia. Circle of confusion — wikipedia, the free encyclopedia, 2015. [Online; accessed December 11, 2015].
- [14] Wikipedia. Hsl and hsv — wikipedia, the free encyclopedia, 2015. [Online; accessed December 11, 2015].
- [15] Giichi Yamamoto. Direct absorption of solar radiation by atmospheric water vapor, carbon dioxide and molecular oxygen. *Journal of the Atmospheric Sciences*, 19(2):182–188, 1962.